University of Central Florida

STARS

2023

Optical Characterization of Liquids: Refractive Index and Raman Gain Coefficient Measurements

Cesar A. Lopez-Zelaya
University of Central Florida

OPTICAL CHARACTERIZATION OF LIQUIDS: REFRACTIVE INDEX AND RAMAN
GAIN COEFFICIENT MEASUREMENTS

by

CESAR A. LOPEZ-ZELAYA
B.S.P.S.E. University of Central Florida, 2021

A thesis submitted in partial fulfilment of the requirements
for the degree of Master of Science
in CREOL, The College of Optics and Photonics
at the University of Central Florida
Orlando, Florida

Fall Term
2023

Major Professor: David J. Hagan

ABSTRACT

Novel technologies capable of generating wavelengths not accessible with typical laser gain media have been among the primary drivers of the field of nonlinear optics. Here, we are interested in the linear and nonlinear properties of liquids beyond the visible spectrum, motivated in part by their use as core materials in optical fibers. Given their dispersion, nonlinearities, transparency, and ability to be mixed, liquids show potential for exploiting in-fiber nonlinear phenomena for developing the new generation of low cost, size, weight, and power wavelength-agile fiber-laser sources. For the design, modeling, and experimental realization of these liquid-core fiber laser sources, proper knowledge of dispersion and Raman gain coefficients is necessary. However, the data for the liquids in the near-IR spectrum are sparse, with most reported values being in the visible and only for commonly used solvents.

In this thesis, we report a Rayleigh interferometry-based refractometer to characterize the refractive index of 26 solvents relative to standard materials at seven different wavelengths (543.5, 632.8, 780, 973, 1064, 1550, and 1970 nm) at a temperature of ~21.3 ± 0.6 °C. The corresponding Sellmeier equations fitted to our data for each liquid are given and compared with previously published literature; percent transmittance data for each liquid are also provided.

Furthermore, we use a well-known technique for obtaining the relative total differential Raman cross-section of eight selected solvents at 532 nm. By measuring and analyzing the solvents' spontaneous Raman emission, we obtain their depolarization ratios, linewidth, and calculate their Raman gain coefficients. With knowledge of the electronic resonance and frequency dependence of the total differential cross-section, extrapolations were used to provide values for the total differential cross-section and gain coefficient at 1064 nm.

To my parents, Cesar and Kenya, my siblings, Alejandro and Valentina, my fiancée Betsy, and above all, God.

"And God said, 'let there be light'; and there was light." – Genesis 1:3

TABLE OF CONTENTS

LIST OF FIGURES

LIST OF TABLES

CHAPTER 1: INTRODUCTION

The field of nonlinear optics deals with the interaction of light with matter at high intensities, where the optical properties of a material depend on the light field [1]. Nonlinear optical phenomena are used in a wide range of applications, including frequency conversion [2, 3], optical communication [4], and quantum information [5, 6]. Among the most promising and challenging aspects of nonlinear optics is to generate light at wavelengths that are not readily available from conventional laser sources, for example the near- to mid-wave infrared regions of the electromagnetic spectrum. These wavelengths and the frequency conversion schemes used to generate them have potential uses in multispectral LiDAR [7], free-space laser communication [8], spectroscopy [9–11], remote sensing [12], and laser surgery [13].

One way to achieve frequency conversion is to use optical fibers as nonlinear media. Optical fibers are an ideal conduit for guiding light given advantages such as low loss, high damage thresholds, long interaction lengths, and straightforward integration with telecommunication systems. Optical fibers, however, are typically made of fused silica, which has a limited transparency range and relatively weak nonlinearities. Therefore, the need for alternative materials capable of extending the performance and functionality of optical fibers for nonlinear applications.

Liquids are an attractive option for nonlinear fiber optics, as they have several desirable properties such as broad transparency range, high nonlinearity, and tunability via their ability to be mixed. Some of their properties, for instance, may be externally tuned with temperature and electrostatic fields. Therefore, architectures taking advantage of the benefits of optical fibers and liquids have potential in being low cost, size, weight, and power alternatives to conventional nonlinear fiber lasers.

It has been shown that liquids can be used to selectively fill specific portions of microstructured

1

fibers [14] and be used as core material in liquid-core fibers [15, 16], where most of the light propagates in the liquid instead of the solid cladding. Additionally, it has been reported that liquid core fibers have been spliced with solid-core optical fibers [17]; thus, demonstrating the ability to be integrated in all-fiber optical setups. Liquid-core fibers have been used for all-optical digital processing [18], supercontinuum generation [19], and multispectral Raman generation [20]. In Fig. 1.1, we show the cascaded spectrum we generated in a (bromotrichloromethane) CBrCl3-filled fiber overlapped with the atmospheric transmission spectrum. The stimulated Raman lines form a ladder of frequencies spaced by ~423 cm^{-1}.
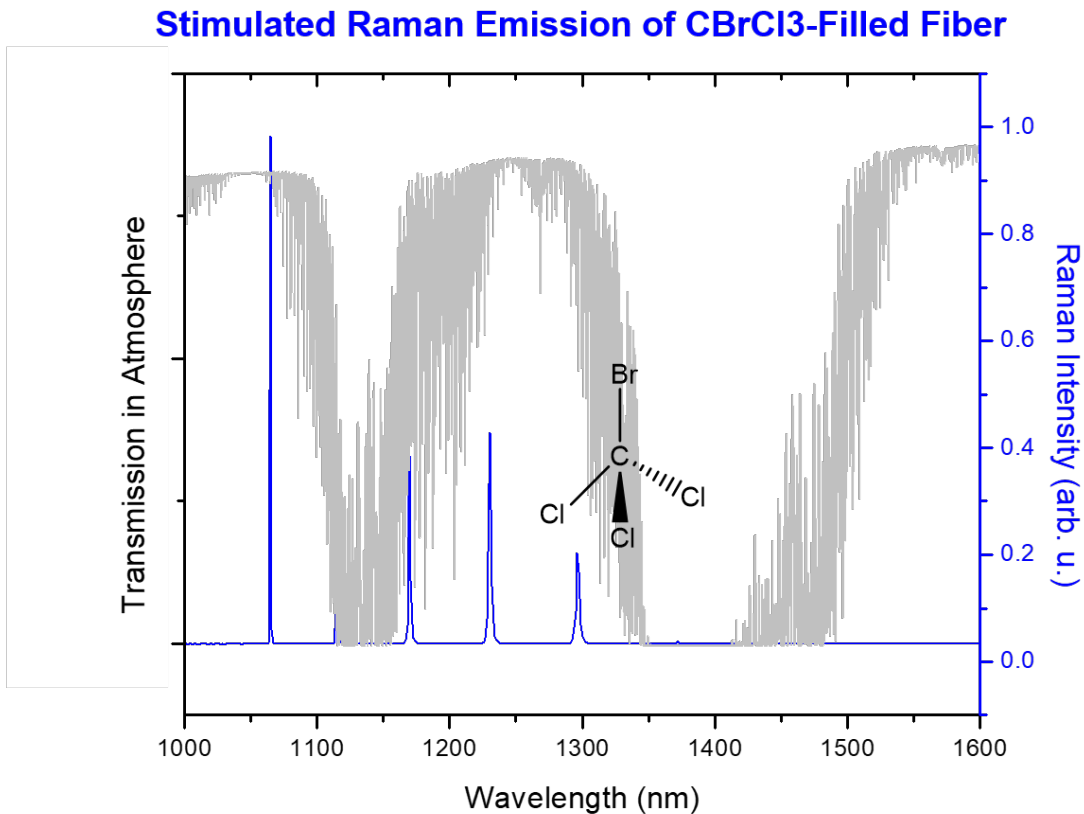
Figure 1.1: Stimulated Raman scattering from a CBrCl3-filled fiber pumped at 1064 nm with 5 ns pulses producing a ladder of frequencies spaced by ~423 cm^{-1} (blue trace). Fiber output is overlayed with atmospheric transmission (gray trace). The molecule depicted is of CBrCl3.

We recently considered CBrCl3, (trichloroacetonitrile) CCl3CN, and (perfluorohexane) C6F14, for a novel quasi-phase-matched liquid-filled fiber optical parametric amplification (QPM-OPA) architecture [21]. These liquids were chosen for their absence of X-H bonds, which in principle should make them more suitable for deeper infrared applications. In our model, applying strong electrostatic fields using periodic electrodes along a 50/50% CBrCl3:CCl3CN liquid-core fiber, we induced an effective second-order nonlinear susceptibility, $\chi_{eff}^{(2)} \propto \chi^{(3)} E_{dc}$, which, in theory, enabled 70% frequency conversion from 1064 nm to 2.128 nm. However, we encountered challenges due to the lack of data on the liquid's absorption coefficients, refractive index dispersion, Raman gain coefficients, and nonlinear susceptibilities were not known. Although absorption spectra [22] and recent absorption coefficient measurements[23] provided some insights, comprehensive knowledge of their properties remained elusive. As shown in Fig. 1.2, knowledge of the Raman gain coefficient is essential to model the onset of stimulated Raman scattering accurately. There is a competition between the gain coefficients from optical parametric amplification and stimulated Raman; thus, determining the Raman gain coefficient is vital to tailor our system to favor optical parametric amplification. Efficient parametric amplification also depends on phase-matching, for which we need dispersion. This, then, has driven our current efforts to measure the liquid's refractive index dispersion from ~400 to ~2000 nm and Raman gain coefficients at 1064 nm.

In this thesis, we present a comprehensive study of the linear and nonlinear optical properties of liquids at and beyond the visible spectrum, with a focus on their use as core materials in optical fibers for frequency conversion. We use two techniques to measure and analyze the optical properties of liquids: Rayleigh interferometry and spontaneous Raman scattering.

In Chapter 2, we use a Rayleigh interferometer -based refractometer to measure the refractive index of 26 solvents relative to standard materials at seven different wavelengths from 543.5 nm to 1970 nm. We also measure the percent transmittance of each solvent at these wavelengths to more qualitatively get an idea of their absorption losses. We fit our data to Sellmeier equations to obtain
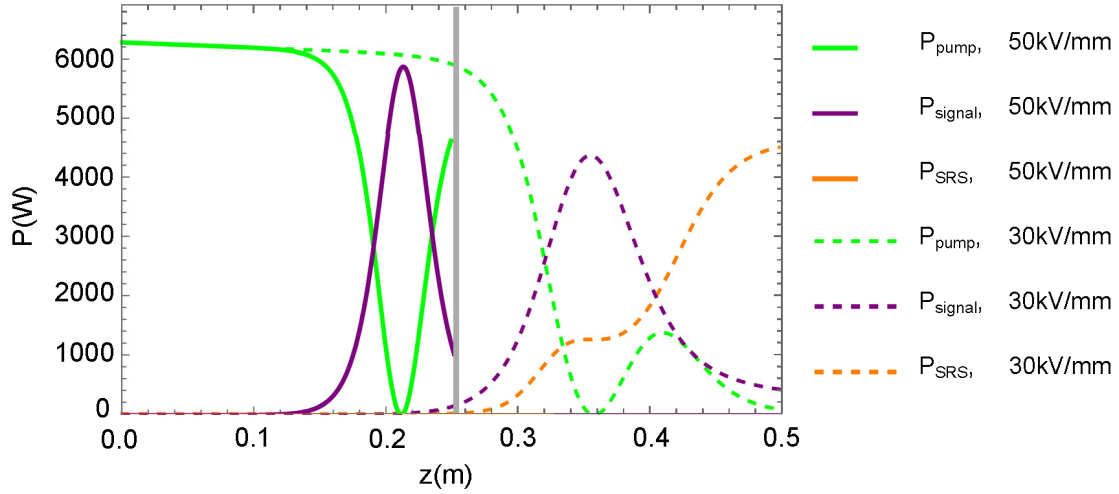
Figure 1.2: Model of QPM-OPA operation with a 50/50% CBrCl3:CCl3CN liquid-core fiber. The pump power at 1064 nm, $P_{pump} = 6.3$ kW, and the 2.128 μm seed signal power, $P_{seed} = 2$ mW. Solid lines are for $E_{dc} = 50$ kV/mm and dashed lines are for $E_{dc} = 30$ kV/mm. (green – pump peak power, purple – signal peak power, orange – stimulated Raman peak power). Parasitic stimulated Raman is generated for $E_{dc} = 30$ kV/mm case. The vertical grey line indicates where we stopped the high field plot case to avoid overlap with the low field case [21].

dispersion relations for each solvent, and compare our results with previously published literature.

In Chapter 3, we use spontaneous Raman scattering to measure the relative total differential Raman cross-section of eight selected solvents at 532 nm. We also obtain their depolarization ratios and linewidths from their Raman spectra. We use these parameters to calculate their Raman gain coefficients at 532 nm and 1064 nm, which are important for stimulated Raman scattering in optical fibers. We also use a theoretical model based on electronic resonance and frequency dependence to extrapolate our results to other wavelengths.

The results of this thesis provide valuable data and insights for the development of liquid-core fiber devices for nonlinear optics and frequency conversion.

CHAPTER 2: REFRACTIVE INDEX MEASUREMENTS USING RAYLEIGH INTERFEROMETRY

Introduction

The development of near-IR fiber laser sources based on liquid-core fiber architectures is a promising research direction in nonlinear optics. However, designing and optimizing such sources requires accurate knowledge of the refractive index and dispersion of the liquid core materials in the near-IR region. While the refractive index of liquids has been extensively studied in the visible region, the refractive index and dispersion of most liquids in the near-IR remains unknown. The lack of both is especially true for hydrogen-free solvents, which can exhibit wide transmission windows in the near-IR due to the absence of vibrational absorption bands [22, 23]. Some notable examples studied here, include carbon tetrachloride, tetrachloroethylene, pentafluorobenzonitrile, bromotrichloromethane, and perfluorohexane. These solvents are good candidates for a wide variety of recent applications such as in liquid-core optical fibers [24–30], supercontinuum generation [31], filamentation [32], design of optofluidic devices [33, 34] and nonlinear optics [35].

Multiple measurement techniques for liquids have been developed, some notable examples include: minimum deviation [36–40], where the liquid is placed in, e.g., a hollow prism, and the refractive index of the liquid is determined from the the minimized angle between the incident beam and the deflected beam. Abbe refractometry [41–43], where the sample is placed in a thin layer between two prisms, one of which is illuminated by a light source and the other of which has a detector behind it. The angle of incidence of the light on the first prism is varied until the light is totally internally reflected at the interface between the sample and the second prism. This angle corresponds to the critical angle, which depends on the refractive index of the sample. By

measuring this angle, the refractive index can be calculated using Snell's law.

Beam displacement [44–46], where the liquid is placed in a cuvette, and a position-sensitive detector is placed in the far field to measure the transmitted beam movement while rotating the cuvette. Ellipsometry [47–49], where real and imaginary parts of the refractive index are obtained from measuring the polarization state change of light at different interfaces, such as air-liquid, prism-liquid, or liquid-solid (e.g., a silicon wafer). Absorption spectra [50], where the dispersion is calculated from the absorption spectrum via Kramers-Kronig relations. Interferometry, where different setups have been developed using, e.g., white light interference by means of Michelson interferometry [51–53], interference between the reflected and transmitted beam from the liquid [54], and interference between a beam passed through the liquid and a beam passed through another material of known index [55–58] – analogous to our present work.

In this chapter, we report the refractive index of 26 solvents measured at seven different wavelengths (543.5, 632.8, 780, 973, 1064, 1550, and 1970 nm) at a temperature of ~21.3 ± 0.6 °C. To measure these indices, we devised a Rayleigh interferometry-based refractometer, which we found to be simple to setup, accurate (depending on curve fitting and the choice of reference), and worked best for our laboratories. Dispersion is reported in the form of Sellmeier equations, which are applicable from 543.5 nm to 1970 nm. We discuss the technique, compare our experimental results with values reported in the literature spanning the range from 400 nm to 2000 nm, and provide percent transmittance spectra for each liquid in that range.

Theory and Experiment

The Rayleigh interferometer used in this work is shown in Fig. 2.1(a). A light beam from a laser source passes through a half-wave plate (HWP) located between a pair of polarizers (P) to control

the power and input polarization. The beam then passes through a spatial filter (SF) to improve its spatial coherence and is collimated by a first lens (L_b) to form a Gaussian beam. The spatial profile when using the 1970 nm laser was good enough to not need a spatial filter. This Gaussian beam passes through an opaque plate with two 0.5 mm holes with a center-to-center distance of $dp \approx 1.3$ mm to produce two beamlets: the reference beam and the sample beam. For both 1550 nm and 1970 nm, a plate with 0.8 mm holes and $dp \approx 2.8$ mm is used. The two beamlets travel alongside each other and are incident onto a Starna 63-Q-10 Spectrosil quartz cuvette, shown in Fig. 2.1(b) (left), with two internal chambers of 10 ± 0.01 mm pathlength. One of the beamlets traverses the center chamber of the cuvette, where the sample liquid is, while the other beamlet goes through the side chamber of the cuvette, where the reference liquid is. Whenever fused silica is used as the reference material, the Starna 29F-Q-10 cuvette, shown in Fig. 2.1(b) (right), with a single 10 ± 0.01 mm pathlength chamber is used. In this case, one of the beamlets goes through the central chamber, where the sample liquid is, while the other beamlet goes through the side fused silica wall, which acts as a chamber filled with glass. The two spatially and temporally coherent beamlets are then weakly focused by the second lens (L_f) to create interference fringes. The focal length of L_f is $f = 1000$ mm for 1064 nm and shorter wavelengths, and $f = 750$ mm for 1550 nm and 1970 nm wavelengths. The interference fringes are measured on one of two cameras, or a detector, depending on the wavelength.

The interference pattern was recorded while the cuvette was rotated to measure the phase difference between the reference and the sample. As the refractive index of the reference and the sample liquid are different, the two beamlets travel different optical paths as shown in Fig. 2.1(b). Hence, the relative phase difference between the beamlets can be written as:

$$\Delta\phi(\theta_{in}) = \frac{2\pi}{\lambda_0}\left[L\sqrt{n_{sam}^2 - \sin^2\theta_{in}} + F_{sam}(\theta_{in}) - L\sqrt{n_{ref}^2 - \sin^2\theta_{in}} - F_{ref}(\theta_{in}) - \Delta\phi_0\right], \quad (2.1)$$

7

(a) Top View

(b) Side View   **(c)** Lens, L_f
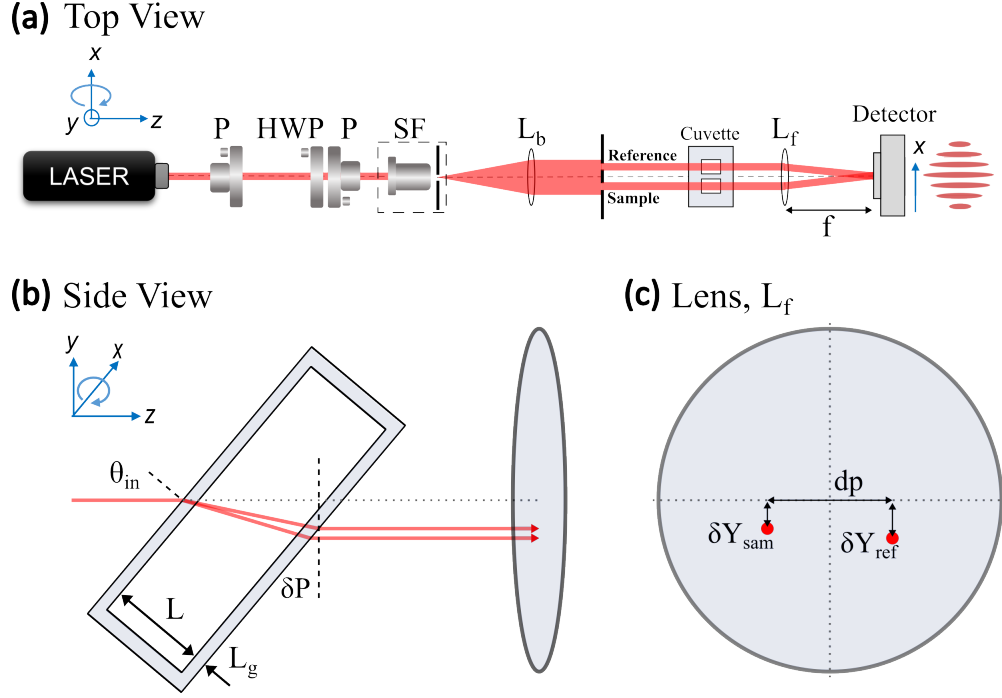
Figure 2.1: (a) Top view of the Rayleigh interferometer. (b) Side view of the rotated cuvette with beamlets incident at an angle θ_{in}. The beamlets refract at different angles and experience different optical paths due to the refractive indices of the sample, n_{sam}, and reference, n_{ref}, refractive indices. (c) Consequently, the beamlets become vertically misaligned on the second lens, L_f, by δY_{sam} and δY_{ref}.

where θ_{in} is the angle of incidence, λ_0 is the free-space wavelength, n_{sam} and n_{ref} are the sample and reference refractive indices, respectively, and $F_{sam}(\theta_{in}) = \sqrt{(dp/2)^2 + \delta Y_{sam}(\theta_{in})^2 + f^2}$ and $F_{ref}(\theta_{in}) = \sqrt{(dp/2)^2 + \delta Y_{ref}(\theta_{in})^2 + f^2}$ are the paths of the beamlets to either a camera or detector depending on the wavelength. As the cuvette is rotated, the beamlets undergo different displacements due to refraction. These displacements, $\delta Y_{sam}(\theta_{in})$ and $\delta Y_{ref}(\theta_{in})$, cause one of the beamlets to exit the cuvette first, resulting in an additional pathlength, $\delta P(\theta_{in})$, as shown in Fig.2.1(b). Additionally, those same displacements cause the beamlets to become misaligned on the second lens, L_f, as shown in Fig.2.1(c). The expressions for $\delta Y_{sam}(\theta_{in})$ and $\delta Y_{ref}(\theta_{in})$ were derived in [44] and are given by: $\delta Y_{sam}(\theta_{in}) = \left[2L_g \left(1 - \frac{\cos\theta_{in}}{\sqrt{n_g^2 - \sin^2\theta_{in}}} \right) + L \left(1 - \frac{\cos\theta_{in}}{\sqrt{n_{sam}^2 - \sin^2\theta_{in}}} \right) \right] \sin\theta_{in}$, where

$L_g = 1.25$ mm is the thickness of the cuvette walls, and n_g is the refractive index of Spectrosil quartz at a specific wavelength; a similar expression where n_{ref} is used instead corresponds to $\delta Y_{ref}(\theta_{in})$. Note that the rightmost term in Eq. 2.1, $\Delta\phi_0 = Ln_{sam} - Ln_{ref}$, is included to ensure $\Delta\phi(0°) = 0$.

In Fig. 2.1(b) and (c), the beam separations are greatly exaggerated to show the pathlength differences. In actuality, assuming $\theta_{in} = 20°$, $n_{sam} > n_{ref}$ and $n_{sam} - n_{ref} \leq 0.1$, the maximum angle difference due to refraction is $\theta_{ref} - \theta_{sam} \approx 1°$. The difference in the vertical displacement of the two beamlets is $\Delta Y(20°) = \delta Y_{sam}(20°) - \delta Y_{ref}(20°) \approx 200$ µm, as shown greatly exaggerated in Fig. 2.1(b) and (c), which can lead to a slight xy-plane twist of the fringes by an angle $\theta_{twist} = \tan^{-1}(\Delta Y(20°)/dp) \leq 10°$. Note that this fringe twisting effect is most noticeable at large θ_{in}, thus justifying it being neglected in the case of this work.

The phase difference, $\Delta\phi$, will change with incident angle, causing the interference fringes to move. Fig. 2.2 shows the interferogram between a cyclohexane sample and Fused Silica Matching Liquid Code 50350 as the reference. Fig. 2.2(a) shows the cross-section of interference fringes as a function of position on the camera for several different incident angles. As shown in the figure, the interference maxima move as the cuvette is rotated. Fig. 2.2(b) shows the positions of the maxima as a function of incident angle. The solid lines in Fig. 2.2(b) represent the optimal fit to Eq. 2.1 based on the data, where the adjustable factors are n and the angle of normal incidence.

The complete optical setup is shown in Fig. 2.3. Seven laser sources were used: two helium-neon lasers with central wavelengths at 543.5 nm (Melles Griot, 05-LGR-025-S) and 632.8 nm (Melles Griot, 05-LHP-171), two diode lasers with central wavelengths at 780 nm and 973 nm (the wavelength was measured with an Ocean Optics spectrometer), a microchip laser (teemPhotonics, MLC-0240DR1) at 1064 nm, a laser diode module (Thorlabs, LDM1550) at 1550 nm and a thulium fiber laser (AdValue, AP-QS-MOD) at 1970 nm. The detectors are a silicon beam pro-
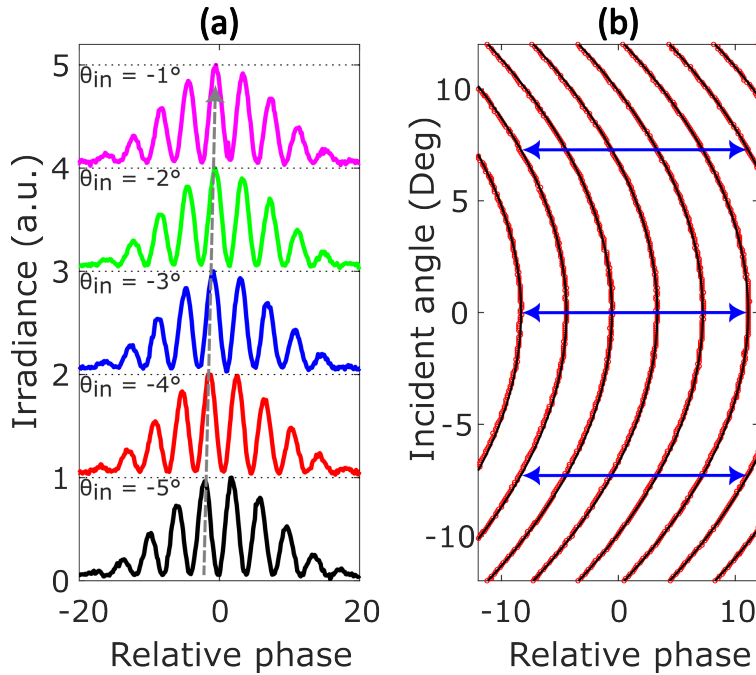
Figure 2.2: (a) Cross-section of the interference fringes at different incident angles for cyclohexane using fused silica index matching liquid as a reference at 543.5 nm. Gray dashed arrow represents fringe displacement. (b) Interference maxima plotted vs. incident angle from camera image (red points) along with fits to Eq. 2.1 (black curves). Blue horizontal arrows of equal length represent a 10π relative phase.

filer (Coherent, LASERCAM HR) for the shortest five wavelengths, an InGaAs camera (Sensors Unlimited, SU640CSX) for 1550 nm, and a 20 um pinhole attached to a PbSe detector (Thorlabs, PDA20H) for 1970 nm. The silicon beam profiler was used to generate the full fringe trajectory pattern shown in Fig. 2.2(b). This pattern was generated through repeated scans at various incident angles, a process that only required a few minutes. Similarly, employing the InGaAs camera at 1550 nm to generate equivalent patterns also took only a few minutes. In contrast, scans with the PbSe detector at 1970 nm took ~12 hours. For instance, when examining trichloroacetonitrile at 1970 nm, the interference fringes were scanned across 161 detector positions for each of the 151 incident angles. For the angular rotations, a Newport universal motion controller driver model ESP300 was used. The temperature is measured by an external thermometer (Xsensior). All mea-

surements are done at ~21.3 $\pm$ 0.6 °C. All the solvents are commercially available as referenced in Tables 2.3-2.6, and used without further purification.
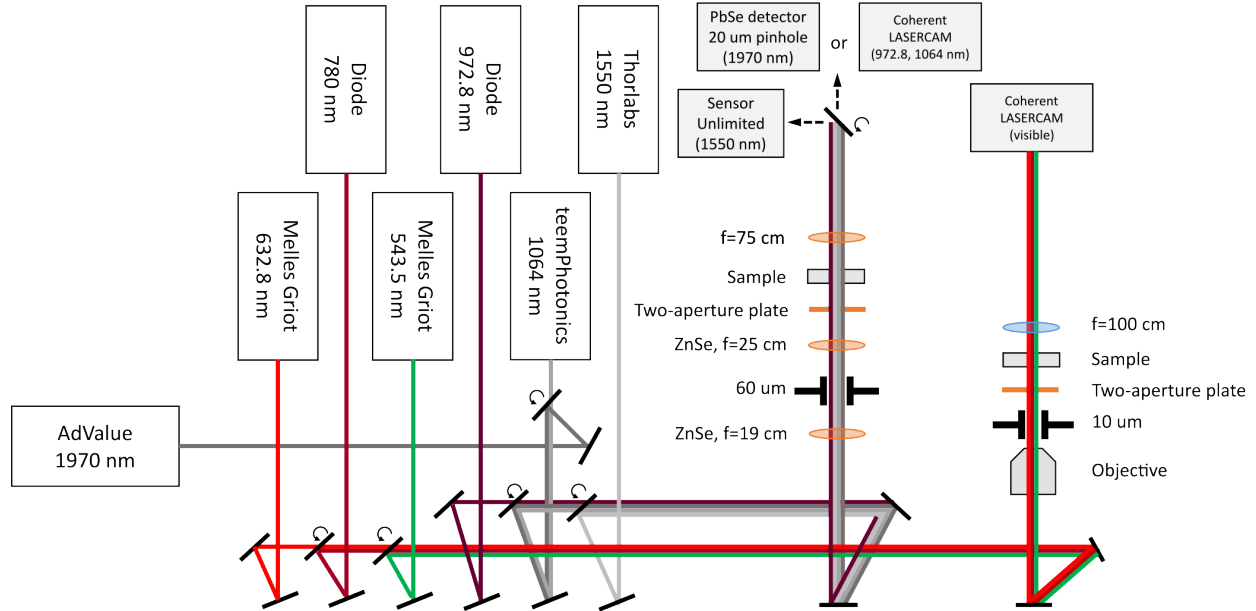
Figure 2.3: Experimental setup for measuring the refractive indices reported in this work [59].

The reference materials are the 29F-Q-10 cuvette wall (Spectrosil quartz from Heraeus) and refractive index liquids from Cargille labs loaded on the side channel of the 63-Q-10 cuvette. The dispersion relationship of Suprasil quartz from Heraeus at 20°C is given by the following Sellmeier equation:

$$n^2 - 1 = \frac{B_1\lambda^2}{\lambda^2 - C_1} + \frac{B_2\lambda^2}{\lambda^2 - C_2} + \frac{B_3\lambda^2}{\lambda^2 - C_3}, \tag{2.2}$$

where B_i and C_i are dispersion constants shown in Table 2.1, and λ is the wavelength in μm. The thermo-optic coefficient, dn/dT, is in the order of 10^{-5} K^{-1}.

The dispersion relationship of the index matching liquids from Cargille labs at 25°C is given by the following Cauchy formula:

$$n = A + \frac{B}{\lambda^2} + \frac{C}{\lambda^4}, \tag{2.3}$$

11

Table 2.1: Dispersion constant for Suprasil and Infrasil quartz from Heraeus

Dispersion constant	Suprasil	Infrasil
B_1	$4.73115591 \times 10^{-1}$	$4.76523070 \times 10^{-1}$
B_2	$6.31038719 \times 10^{-1}$	$6.27786368 \times 10^{-1}$
B_3	$9.06404498 \times 10^{-1}$	$8.72274404 \times 10^{-1}$
C_1	$1.29957170 \times 10^{-2}$	$2.84888095 \times 10^{-3}$
C_2	$4.12809220 \times 10^{-3}$	$1.18369052 \times 10^{-2}$
C_3	9.87685322×10^{1}	9.56856012×10^{1}

where A and B are dispersion constants shown in Table 2.2, and λ is the wavelength in nm. The thermo-optic coefficients, dn/dT, from 15°to 35°C for the series AAA 1.30000 and series AA 1.41000, and Liquid code 50350 are -3.33, -4.08, and -3.86×10^{-4} K^{-1}, respectively.

Table 2.2: Dispersion constants for Cargille labs refractive index liquids

Dispersion constant	Series AAA 1.30000	Series AA 1.41000	Liquid code 50350
A	1.293552	1.397927	1.44690
$B(\times 10^3)$	2.6171	4.2805	3.98963
$C(\times 10^7)$	-1.3126839	-3.0544326	3.75775

Results

The experimental results are presented in 2.3-2.6 along with literature data. The first column lists the liquids being characterized, their chemical formulas, and the vendors we obtained them from. Parentheses in the third and fourth column show the temperature and index measurement uncertainty ($\pm$) in the 4th decimal. The two major contributions to the measurement uncertainty are the fitting error and the uncertainty of the reference material's refractive index. A star (*) in the literature column indicates that the value is calculated from the dispersion function reported in the corresponding literature. Double stars (**) in Ref. [50] indicate values calculated from

Kramers-Kronig relations. The reference refractive index for each sample was typically chosen to yield an index difference, $|n - n_{ref}|$, between ~0.01 and 0.1 to better fit Eq. 2.1 to them, such as in Fig. 2.2(b). Figs. 2.4-2.8 show the % transmittance spectrum for each sample measured with a Cary 500 spectrophotometer from 400 to 2000 nm. The transmittance spectrum for each sample includes the reflection loss from the 10 mm pathlength Spectrosil quartz cuvette. The absorption of the cuvette at this wavelength region is negligible.
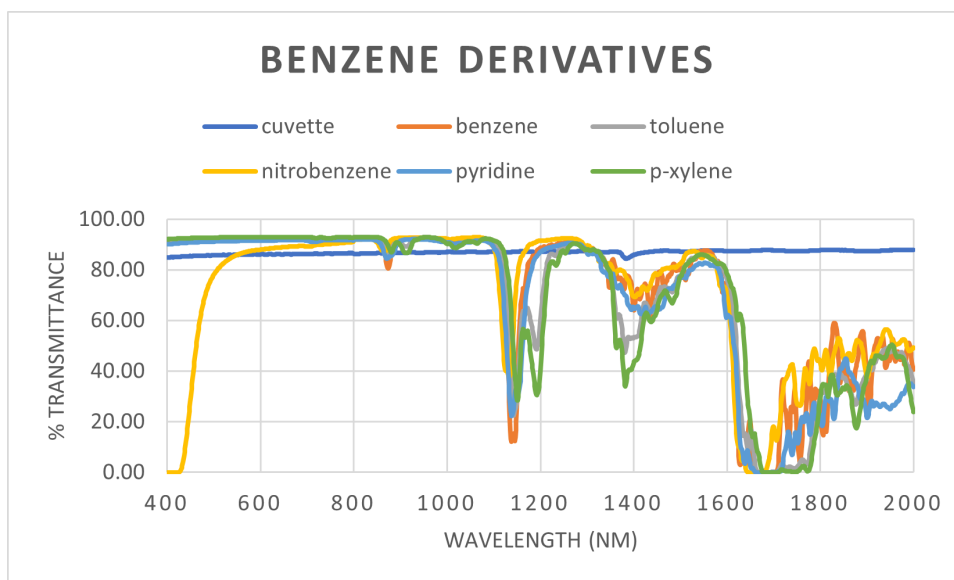
Figure 2.4: Percent transmittance of various benzene derivatives.
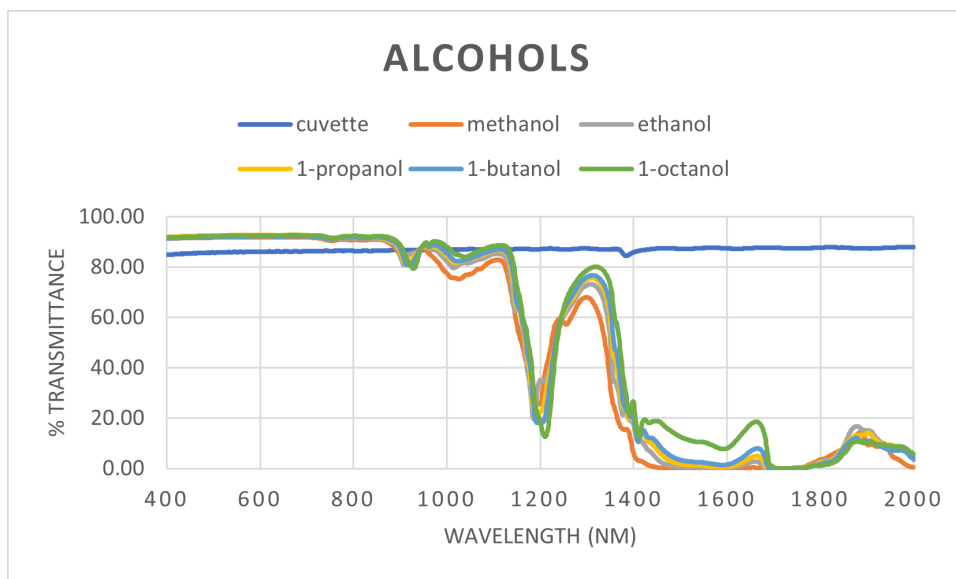
Figure 2.5: Percent transmittance of various alcohols.
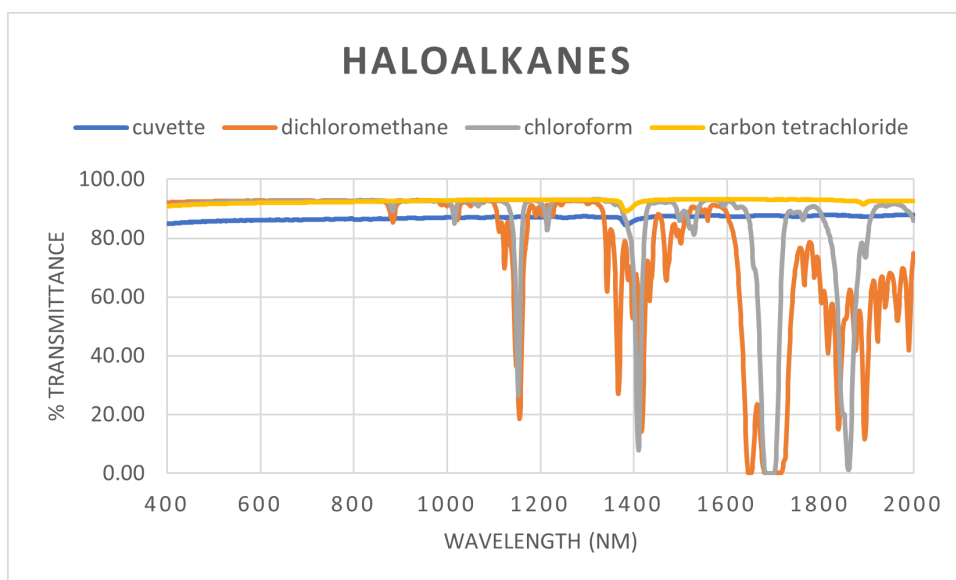
Figure 2.6: Percent transmittance of various haloalkanes.
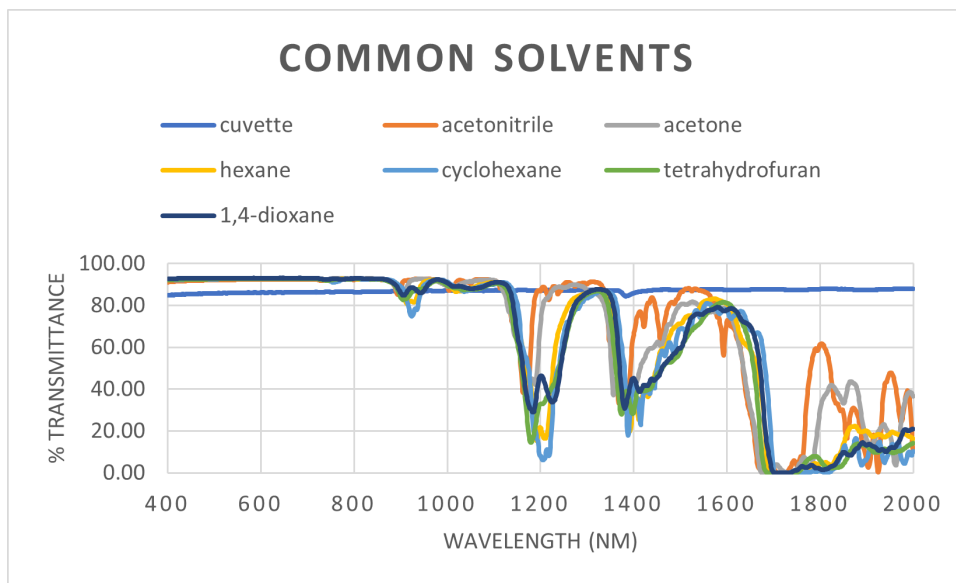
Figure 2.7: Percent transmittance of various common solvents.
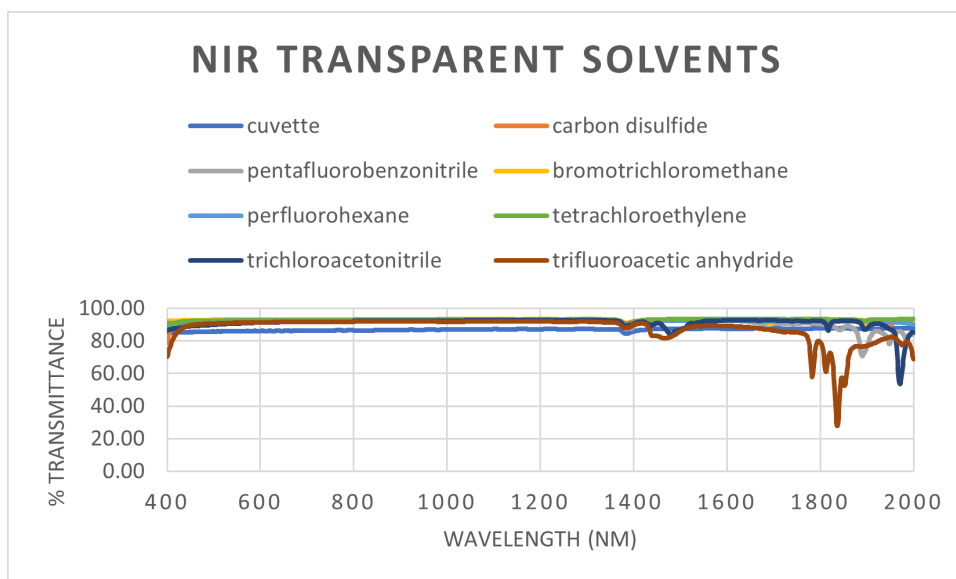
Figure 2.8: Percent transmittance of various near-IR transparent solvents.

Table 2.3: Refractive index of benzene derivatives in this work and literature

Molecule	Wavelength (nm)	This work	Literature
Benzene (C_6H_6) (Sigma-Aldrich)	543.5	1.5037(21,5)	1.4999(27)[60], 1.5055(20)[55], 1.5056(20)[61]*,
	632.8	1.4964(21,5)	1.4925(27)[60]*, 1.495137(25)[58]*, 1.497866(20)[55]* 1.4980(20)[61]
	780	1.4888(21,2)	1.4859(27)[60], 1.4908(20)[61]
	973	1.4843(21,10)	1.4815(27)[60], 1.4857(20)[61]
	1064	1.4842(21,10)	1.4802(27)[60], 1.4814(25,1)[46]*, 1.4808(25,5)[46]*, 1.4841(20)[61]
	1550	1.4797(21,3)	1.4769(27)[60]*, 1.4789(25,3)[43], 1.4767(27)[50]*, 1.4777(27)[50]**, 1.4799(20)[61]
	1970	1.4780(21,6)	1.4774(27)[50]**, 1.4784(20)[61]
Toluene ($C_6H_5CH_3$) (ACROS)	543.5	1.4993(21,5)	1.4961(27)[60], 1.5009(20)[42], 1.4979(20)[56], 1.5009(20)[61], 1.4996(22)[62]
	632.8	1.4914(21,6)	1.4890(27)[60]*, 1.4936(20)[42], 1.491218(25)[58]*, 1.4936(20)[61], 1.4940(22)[62]
	780	1.4850(21,2)	1.4824(27)[60], 1.4870(20)[42], 1.4869(20)[61]
	973	1.4805(21,10)	1.4781(27)[60], 1.4825(20)[42], 1.4824(20)[61]
	1064	1.4800(21,10)	1.4769(27)[60], 1.4812(20)[42], 1.4784(25,1)[46]*, 1.4777(25,3)[46]*, 1.4811(20)[61]
	1550	1.4768(21,4)	1.4737(27)[60]* , 1.4778(20)[42], 1.4760(25,2)[43], 1.4735(27)[50]*, 1.4777(20)[61]
	1970	1.4753(21,4)	1.4744(27)[50]**, 1.4764(20)[61]
P-Xylene ($C_6H_4(CH_3)_2$) (Sigma-Aldrich)	543.5	1.4976(21,2)	
	632.8	1.4915(21,5)	
	780	1.4867(21,4)	
	973	1.4786(21,10)	
	1064	1.4800(21,10)	
	1550	1.4759(21,3)	1.4753(25,1)[43]
	1970	1.4751(21,4)	
Pyridine (C_6H_5N) (Sigma-Aldrich)	543.5	1.5115(21,6)	
	632.8	1.5038(21,6)	
	780	1.4978(21,3)	
	973	1.4938(21,10)	
	1064	1.4923(21,10)	
	1550	1.4880(21,3)	1.4851(27)[50]*, 1.4857(27)[50]**
	1970	1.4864(21,7)	1.5212(27)[50]**
Nitrobenzene ($C_6H_5NO_2$) (Sigma-Aldrich)	543.5	1.5567(21,6)	
	632.8	1.5462(21,7)	
	780	1.5353(21,5)	
	973	-	
	1064	1.5264(21,10)	1.5262(25,2)[46]*
	1550	1.5223(21,5)	1.4125(25)[63]
	1970	1.5199(21,7)	1.5212(27)[50]**

Table 2.4: Refractive index of haloalkanes in this work and literature

Molecule	Wavelength (nm)	This work	Literature
Dichloromethane (CH_2Cl_2) (Merck KGaA)	543.5	1.4258(21,5)	
	632.8	1.4217(21,3)	
	780	1.4180(21,4)	
	973	-	
	1064	1.4150(21,10)	1.4120(25,6)[46]*
	1550	1.4133(21,2)	1.4124(25,2)[43], 1.4125(25)[63]
	1970	1.4126(21,4)	1.4121(25)[63]
Chloroform ($CHCl_3$) (Sigma-Aldrich)	543.5	1.4472(21,2)	1.4464(20)[42], 1.4520(20)[56], 1.4485(20)[61]
	632.8	1.4436(21,5)	1.3323(20)[42], 1.441415(20)[56]*, 1.4443(20)[61]
	780	1.4380(21,4)	1.4385(20)[42], 1.4401(20)[61]
	973	1.4370(21,10)	1.4361(20)[42], 1.4371(20)[61]
	1064	1.4347(21,10)	1.4354(20)[42], 1.4331(25,4)[46]*, 1.4362(20)[61]
	1550	1.4332(21,10)	1.4334(20)[42], 1.4321(25,1)[43], 1.4337(20)[61]
	1970	1.4315(21,3)	1.4326(20)[61]
Carbon tetrachloride (CCl_4) (Sigma-Aldrich)	543.5	1.4599(21,4)	1.4593(27)[60], 1.4621(20)[42]
	632.8	1.4566(21,4)	1.4551(27)[60]*, 1.4579(20)[42], 1.455852(25)[58]*
	780	1.4522(21,5)	1.4513(27)[60] , 1.4539(20)[42]
	973	1.4510(21,10)	1.4488(27)[60], 1.4521(20)[42]
	1064	1.4498(21,10)	1.4481(27, 1)[60], 1.4504(20)[42], 1.4477(25,2)[46]*, 1.4557(25)[64]
	1550	1.4468(21,1)	1.4464(27)[60]*, 1.4483(20)[42], 1.4530(25)[64]
	1970	1.4457(21,2)	1.4530(25)[64]

17

Table 2.5: Refractive index of alcohols in this work and literature

Molecule	Wavelength (nm)	This work	Literature
Methanol *(CH₃OH)* *(ACROS)*	543.5	1.3292(21,4)	1.3284(27)[60], 1.3376(20)[55], 1.3295(22)[62]
	632.8	1.3270(21,5)	1.3259(27)[60]*, 1.326343(20)[55]*, 1.3270(22)[62]
	780	1.3224(21,5)	1.3234(27)[60]
	973	1.3210(21,10)	1.3215(27)[60]
	1064	1.3190(21,10)	1.3207(27)[60], 1.3198(25,3)[46]*
	1550	-	1.3172(27)[60]*, 1.3174(25,1)[43], 1.4201(26)[50]*, 1.3115(26)[50]**
	1970	1.3164(21,8)	1.3074(26)[50]**
Ethanol *(C₂H₅OH)* *(Sigma-Aldrich)*	543.5	1.3627(21,3)	1.3631(20)[42], 1.3626(22)[62]
	632.8	1.3604(21,3)	1.3603(20)[42], 1.358853(25)[58]*, 1.3593(22)[62]
	780	1.3580(21,6)	1.3575(20)[42]
	973	1.3543(21,10)	1.3554(20)[42]
	1064	1.3548(21,10)	1.3547(20)[42]
	1550	1.3523(21,10)	1.3520(20)[42], 1.3503(25,3)[43], 1.3495(26)[50]*, 1.3474(26)[50]**
	1970	1.3482(21,6)	1.3447(26)[50]**
1-propanol *(C₃H₈O)* *(Sigma-Aldrich)*	543.5	1.3863(21,3)	1.3846(27)[60]
	632.8	1.3828(21,4)	1.3941(27)[60]*, 1.397105(20)[55]*
	780	1.3810(21,5)	1.3913(27)[60]
	973	1.3783(21,10)	1.3890(27)[60]
	1064	1.3783(21,10)	1.3883(27)[60]
	1550	1.3751(21,10)	1.3858(27)[60]*
	1970	1.3725(21,4)	
1-butanol *(C₄H₁₀O)* *(Sigma-Aldrich)*	543.5	1.3999(21,2)	1.3970(27)[60]
	632.8	1.3978(21,2)	1.3941(27)[60]*, 1.397105(20)[55]*
	780	1.3950(21,4)	1.3913(27)[60]
	973	1.3922(21,10)	1.3890(27)[60]
	1064	1.3916(21,10)	1.3883(27)[60]
	1550	1.3890(21,10)	1.3858(27)[60]*
	1970	1.3868(21,6)	
1-octanol *(C₈H₁₈O)* *(Sigma-Aldrich)*	543.5	1.4305(21,2)	
	632.8	1.4273(21,2)	
	780	1.4235(21,4)	
	973	1.4226(21,10)	
	1064	1.4210(21,10)	
	1550	1.4190(21,10)	
	1970	1.4163(21,2)	

Table 2.6: Refractive index of near-IR transparent solvents

Molecule	Wavelength (nm)	This work	Literature
Carbon disulfide (CS$_2$) (Sigma-Aldrich)	543.5	1.6319(21,9)	1.6373(20)[30], 1.6361(20)[42], 1.6367(20)[61]
	632.8	1.6177(21,10)	1.6213(20)[30], 1.6211(20)[42], 1.617672(25)[58]*, 1.6212(20)[61]
	780	1.6019(21,11)	1.6066(20)[30], 1.6072(20)[42], 1.6069(20)[61]
	973	-	1.5968(20)[30], 1.5981(20)[42], 1.5974(20)[61]
	1064	1.5950(21,10)	1.5939(20)[30], 1.5955(20)[42], 1.5910(25,3)[46]*, 1.5946(20)[61]
	1550	1.5834(21,7)	1.5857(20)[30], 1.5885(20)[42], 1.5872(20)[61]
	1970	1.5802(21,10)	1.5812(20)[30], 1.5843(20)[61]
Pentafluorobenzonitrile (C$_6$F$_5$CN) (Aldrich)	543.5	1.4453(21,5)	
	632.8	1.4381(21,2)	
	780	1.4332(21,3)	
	973	1.4295(21,10)	
	1064	1.4240(21,10)	1.4254(25,4)[46]*
	1550	1.4241(21,4)	
	1970	1.4213(21,4)	
Bromotrichloromethane (BrCCl3) (Sigma-Aldrich)	543.5	1.5080(21,6)	
	632.8	1.5016(21,5)	
	780	1.4958(21,2)	
	973	-	
	1064	1.4932(21,10)	
	1550	1.4895(21,3)	
	1970	1.4881(21,6)	
Perfluorohexane (C$_6$F$_{14}$) (Alfa Aesar)	543.5	1.2524(21,4)	
	632.8	1.2509(21,4)	
	780	1.2495(21,6)	
	973	1.2480(21,10)	
	1064	1.2480(21,10)	
	1550	1.2475(21,10)	
	1970	1.2466(21,11)	
Tetrachloroethylene (C$_2$Cl$_4$) (Sigma-Aldrich)	543.5	1.5068(21,6)	
	632.8	1.5015(21,3)	
	780	1.4955(21,3)	
	973	1.4917(21,10)	
	1064	1.4907(21,10)	
	1550	1.4879(21,4)	
	1970	1.4864(21,5)	
Trichloroacetonitrile (C$_2$Cl$_3$N) (Sigma-Aldrich)	543.5	1.4382(21,4)	
	632.8	1.4348(21,6)	
	780	1.4318(21,6)	
	973	-	
	1064	1.4280(21,9)	
	1550	1.4258(21,11)	
	1970	1.4265(21,10)	
Trifluoroacetic anhydride (C$_4$F$_6$O$_3$) (Sigma-Aldrich)	543.5	1.2708(21,5)	
	632.8	1.2685(21,3)	
	780	1.2661(21,5)	
	973	-	
	1064	1.2645(21,6)	
	1550	1.2641(21,9)	
	1970	1.2628(21,10)	

Table 2.7: Refractive index of other common solvents

Molecule	Wavelength(nm)	This work	Literature
Acetone (C_3H_6O) *(Sigma-Aldrich)*	543.5	1.3590(21,5)	
	632.8	1.3568(21,4)	
	780	1.3525(21,5)	
	973	1.3520(21,10)	
	1064	1.3490(21,10)	1.3487(25,4)[46]*
	1550	1.3487(21,10)	1.3483(25,2)[43]
	1970	1.3477(21,6)	
Acetonitrile (C_2H_3N) *(Sigma-Aldrich)*	543.5	1.3440(21,3)	1.3418(27)[60], 1.3438(22)[62]
	632.8	1.3416(21,6)	1.3393(27)[60]*, 1.3408(22)[62]
	780	1.3395(21,5)	1.3373(27)[60]
	973	1.3365(21,10)	1.3361(27)[60]
	1064	1.3357(21,10)	1.3357(27)[60], 1.3354(25,3)[46]*
	1550	1.3358(21,10)	1.3345(27)[60]*, 1.3335(26)[50]*, 1.3337(26)[50]**, 1.3348(25,2)[43]
	1970	1.3339(21,7)	1.3335(26)[50]**
Hexane (C_6H_{14}) *(Sigma-Aldrich)*	543.5	1.3770(21,4)	1.3776(22)[62]
	632.8	1.3736(21,3)	1.3743(22)[62]
	780	1.3712(21,5)	
	973	1.3688(21,10)	
	1064	1.3698(21,10)	
	1550	1.3670(21,10)	
	1970	1.3668(21,3)	
Cyclohexane (C_6H_{12}) *(ACROS)*	543.5	1.4268(21,3)	1.4273(22)[62]
	632.8	1.4242(21,2)	1.4238(22)[62]
	780	1.4215(21,4)	
	973	1.4185(21,10)	
	1064	1.4180(21,10)	1.4158(25,4)[46]*
	1550	1.4158(21,3)	1.4147(25,11)[43]
	1970	1.4147(21,4)	
Tetrahydrofuran (C_4H_8O) *(ACROS)*	543.5	1.4084(21,2)	
	632.8	1.4053(21,2)	
	780	1.4025(21,3)	
	973	1.4008(21,10))	
	1064	1.4000(21,10)	1.3974(25,1)[46]*
	1550	1.3983(21,10)	1.3969(25,3)[43]
	1970	1.3961(21,4)	
1,4-Dioxane $(C_4H_8O_2)$ *(Sigma-Aldrich)*	543.5	1.4241(21,3)	1.4219(27)[60]
	632.8	1.4197(21,5)	1.4190(27)[60]*
	780	1.4179(21,3)	1.4165(27)[60]
	973	1.4148(21,10)	1.4148(27)[60]
	1064	1.4150(21,10)	1.4143(27)[60], 1.4119(25,2)[46]*
	1550	1.4123(21,10)	1.4124(27)[60]*, 1.4127(25, 5)[43]
	1970	1.4108(21,4)	

For some of the liquids, particularly acetone and acetonitrile, notable variations in the measured index were observed near strong absorption bands. In other cases, despite absorption, the measured indices were fit with a single UV Sellmeier term (e.g., toluene), while in other cases, the IR term was included to improve fitting at longer wavelengths (e.g., most of the alcohols). Despite the high loss due to absorption of some liquids at specific wavelengths, such as 1550 nm for the alcohols, the refractive index could still be measured (albeit with slightly higher uncertainty) with a fringe peak-to-minimum contrast as low as 0.7% – corresponding to ethanol. Ideally, from the equation of interference of two beams (assuming monochromatic plane-waves), we expect a ~20% fringe contrast for ~1% transmission through the liquid. Methanol, on the other hand, exhibits higher absorption at 1550 nm, and thus the fringe contrast was beyond what the InGaAs camera could resolve. In principle, a neutral density filter could be introduced in the reference arm to increase the contrast; however, this was not needed to keep our errors lower than the errors in our reference materials except perhaps for methanol at 1550nm. We did not attempt this due to the added complexity. With acetonitrile, one of the materials that exhibits high loss, we performed experiments at three different power levels (25%, 50%, and 75% of max) at 1970 nm and did not observe any difference in the measured index values that could arise from heating and thermal expansion.

Dispersion relations are obtained by fitting the Sellmeier equation:

$$n^2 - 1 = \frac{B_{UV}\lambda^2}{\lambda^2 - \lambda_{UV}^2} + \frac{B_{IR}\lambda^2}{\lambda^2 - \lambda_{IR}^2} \tag{2.4}$$

to the measured indices. In Eq. 2.4, B_{UV} and B_{IR} are Sellmeier coefficients and λ_{UV} and λ_{IR} are resonances in the UV and IR, respectively. Fits were obtained by using Wolfram Mathematica's "NonlinearModelFit" command with the Levenberg–Marquardt method. The fitting algorithm automatically solved for B_{UV}, B_{IR}, and λ_{UV} resonances, while λ_{IR} resonances were manually set

to the strongest molecular vibration beyond 1970 nm obtained from NIST [65] and AIST [66]. Table 2.8 shows the Sellmeier coefficients and resonances, in nanometers (nm), obtained by only fitting the data we measured. Note that we extended these Sellmeier fits from 543.5 nm down to 400 nm with dotted lines for comparison with literature experimental values; the uncertainty of results extrapolated down to 400 nm is ~5 to 6 times greater than the uncertainty of the measured data. In Figs. 2.9-2.13 we compare our Sellmeier fits and measured indices with data from Landolt–Börnstein [67] and from the broader literature (see Tables 2.3–2.7 and the cited publications, excluding the starred values). We focus on literature data at wavelengths from 400 nm to 2000 nm, and temperatures from 15 °C to 25 °C.

Table 2.8: Sellmeier coefficients and resonances

Solvent	B_{UV}	λ_{UV}	B_{IR}	λ_{IR}
Benzene	1.180	138	-	-
Toluene	1.171	134	-	-
p-Xylene	1.170	133	-	-
Pyridine	1.206	135	-	-
Nitrobenzene	1.302	159	-	-
Dichloromethane	0.9923	107	-	-
Chloroform	1.047	114	-	-
Carbon tetrachloride	1.094	99.6	0.2902	12900
Methanol	0.7316	119	-	-
Ethanol	0.8312	96.4	0.01919	2970
1-Propanol	0.8940	94.4	0.01584	2970
1-Butanol	0.9314	95.9	0.01365	2970
1-Octanol	1.013	96.5	0.01119	2900
Carbon disulfide	1.502	169	0.1634	6520
Pentafluorobenzonitrile	1.017	140	-	-
Bromotrichloromethane	1.211	120	-	-
Perflourohexane	0.5536	88.6	-	-
Tetrachloroethylene	1.206	124	-	-
Trichloroacetonitrile	1.030	103	-	-
Trifluoroacetic Anhydride	0.5939	99.7	-	-
Acetone	0.8144	108	-	-
Acetonitrile	0.7786	102	-	-
Hexane	0.8660	98.8	-	-
Cyclohexane	1.004	97.1	0.01080	3450
Tetrahydrofuran	0.9544	93.5	0.01465	3450
1,4-Dioxane	0.9937	98.2	0.01209	3450
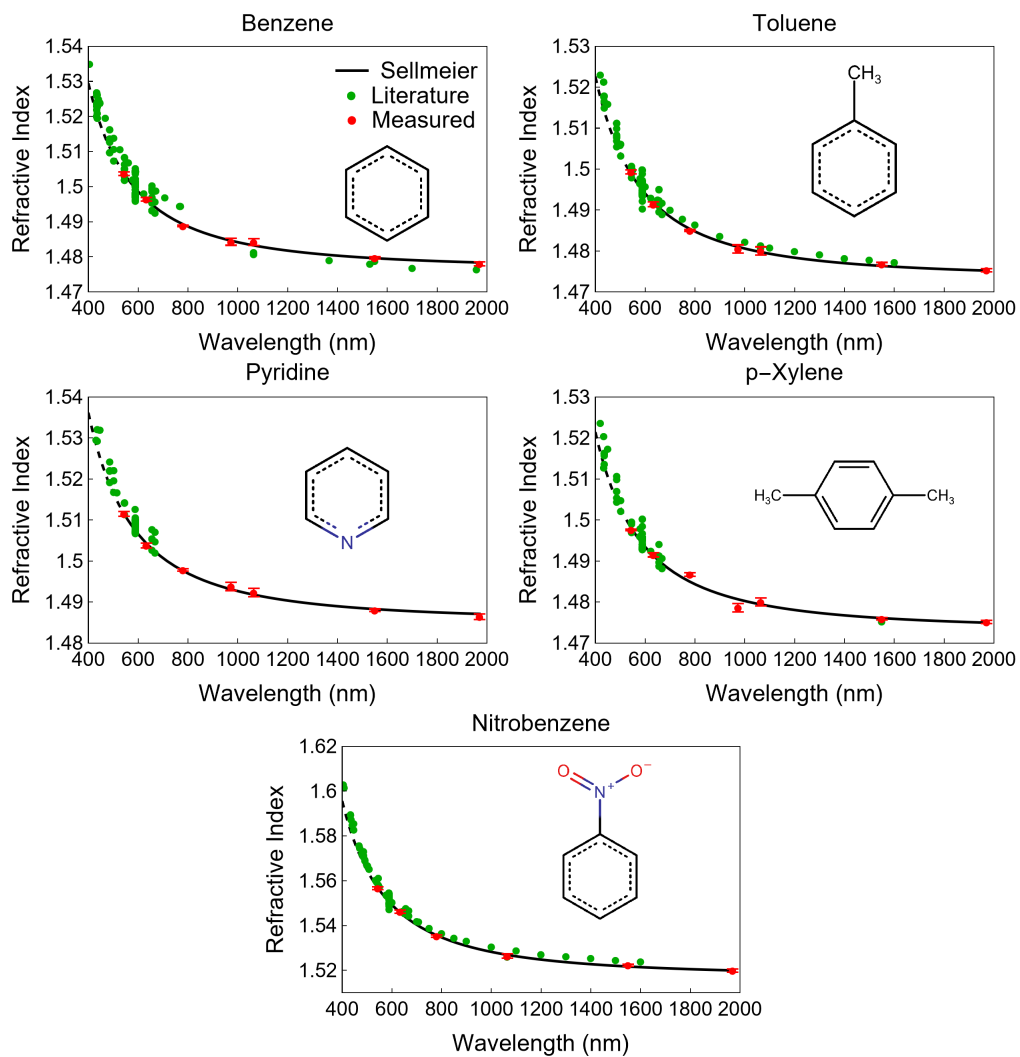
Figure 2.9: Refractive indices reported in this work (red markers), in literature (green markers), and Sellmeier fits to our data and extrapolation (solid and dashed black traces, respectively) for benzene derivatives.
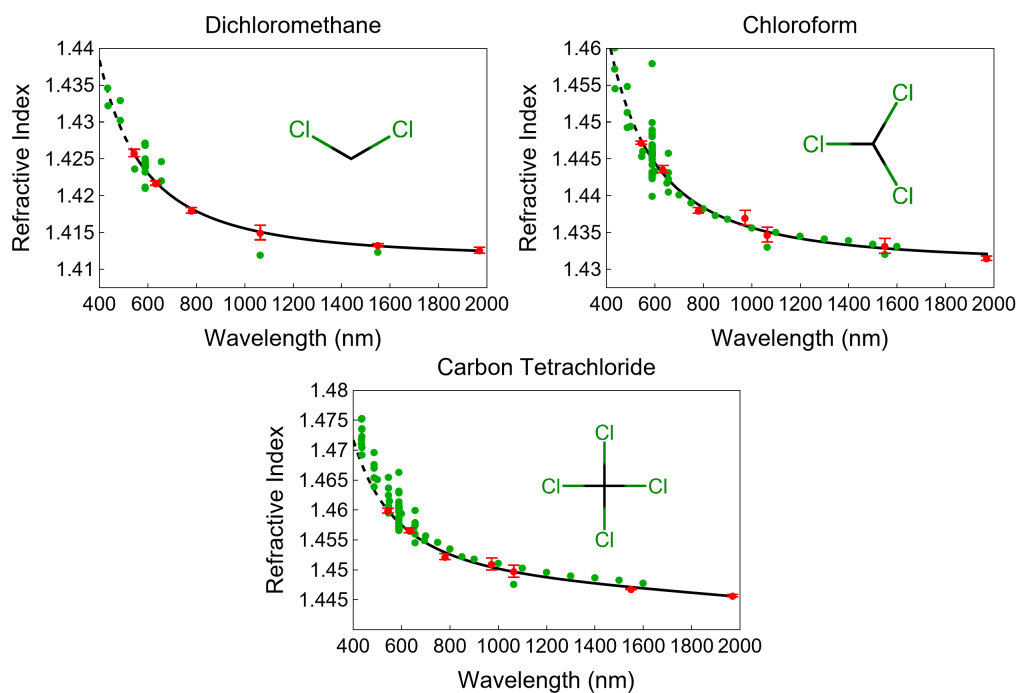
Figure 2.10: Refractive indices reported in this work (red markers), in literature (green markers), and Sellmeier fits to our data and extrapolation (solid and dashed black traces, respectively) for haloalkanes.
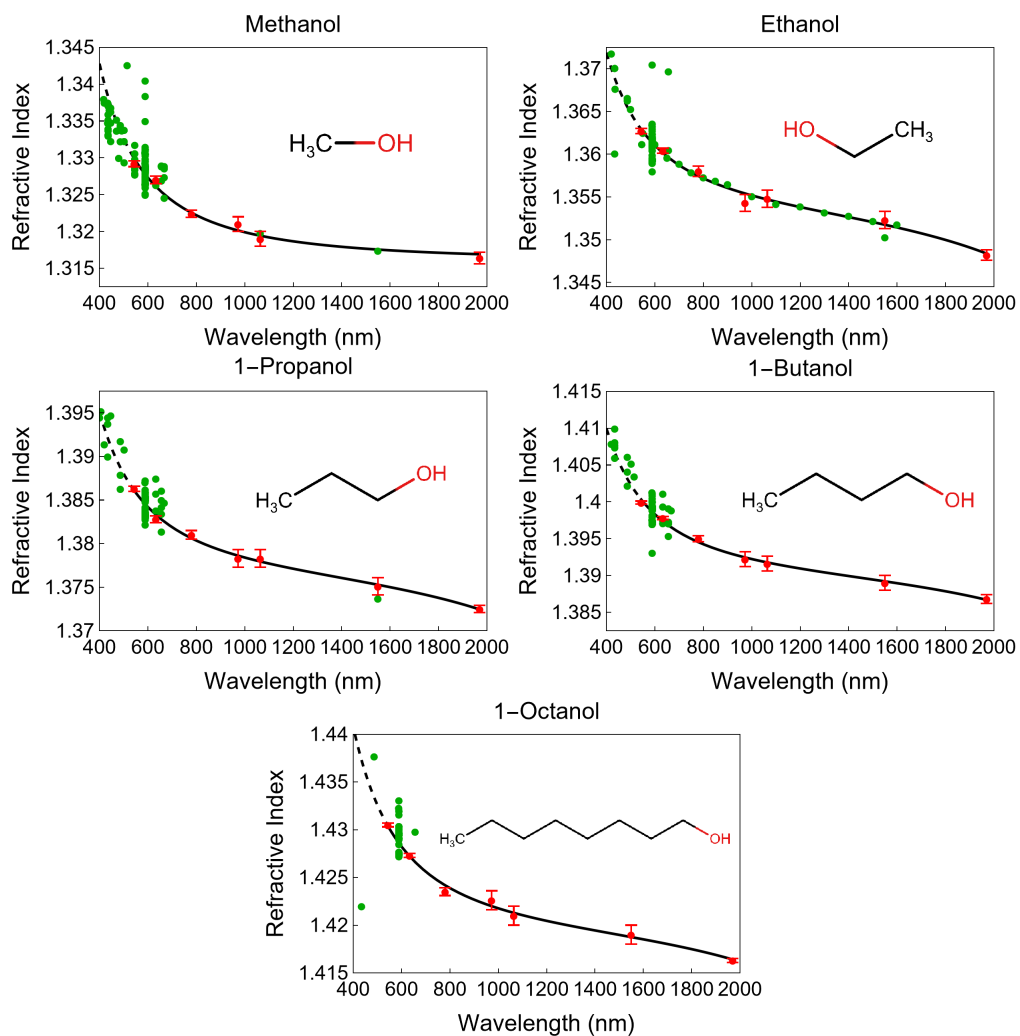
Figure 2.11: Refractive indices reported in this work (red markers), in literature (green markers), and Sellmeier fits to our data and extrapolation (solid and dashed black traces, respectively) for alcohols.
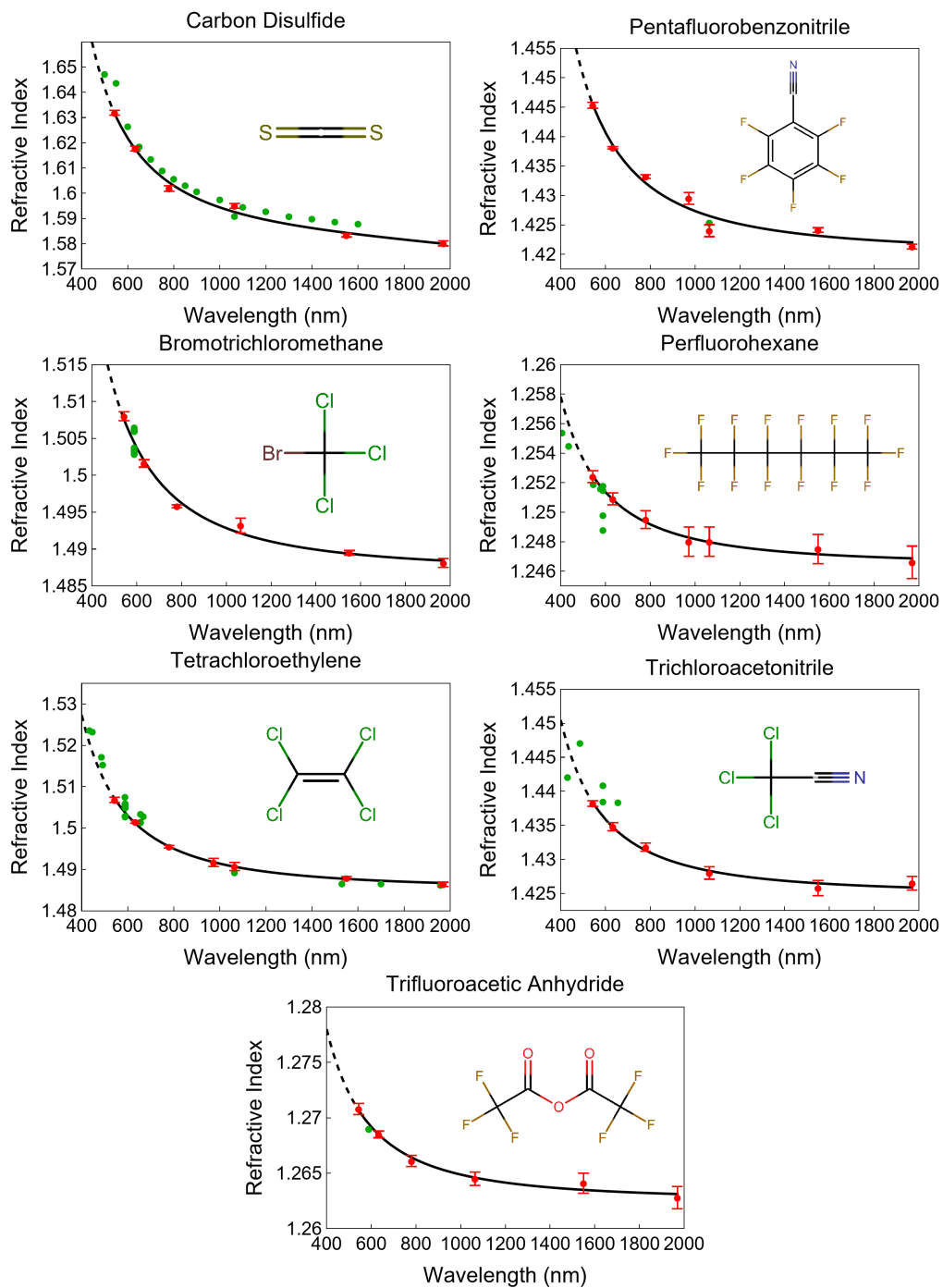
Figure 2.12: Refractive indices reported in this work (red markers), in literature (green markers), and Sellmeier fits to our data and extrapolation (solid and dashed black traces, respectively) for near-IR transparent solvents.
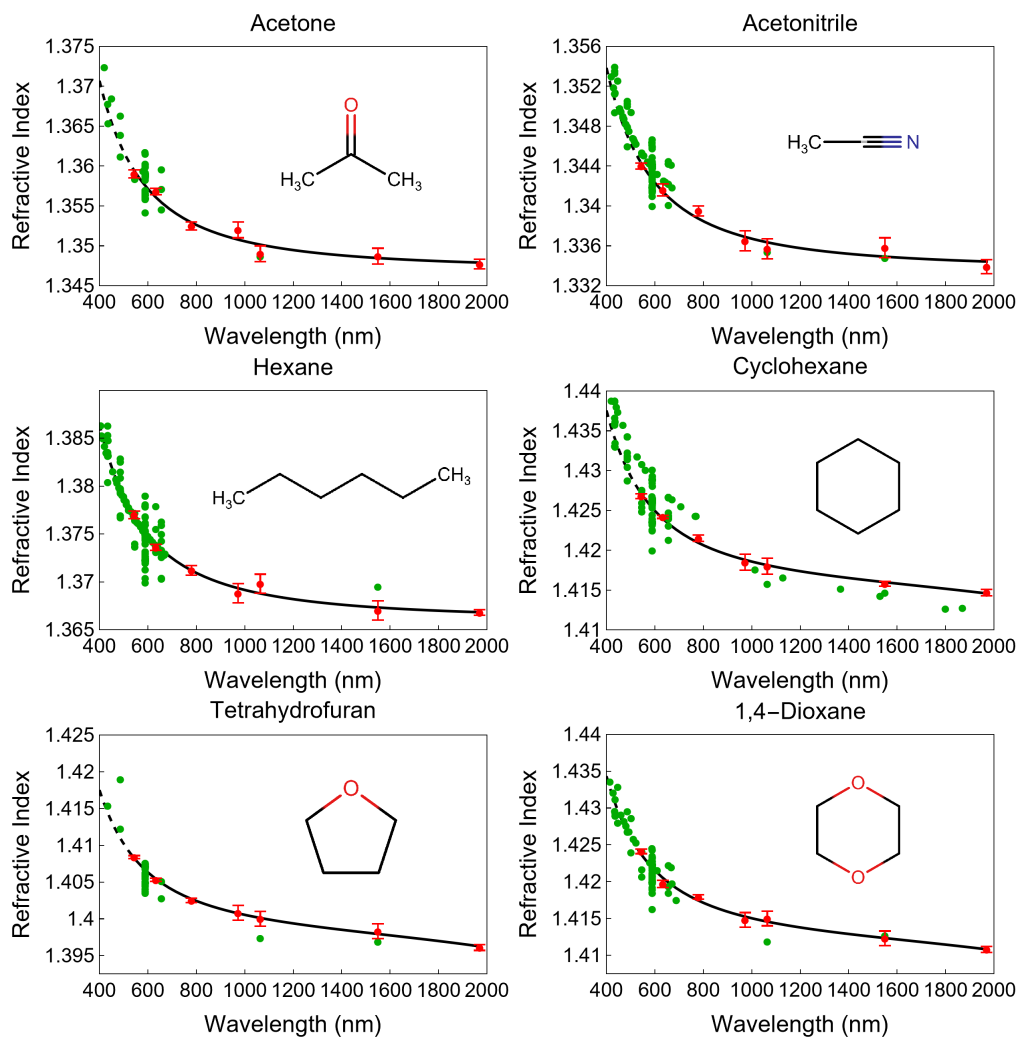
Figure 2.13: Refractive indices reported in this work (red markers), in literature (green markers), and Sellmeier fits to our data and extrapolation (solid and dashed black traces, respectively) for common solvents.

CHAPTER 3: STIMULATED RAMAN GAIN MEASUREMENTS FROM SPONTANEOUS RAMAN SCATTERING

Introduction

Spontaneous Raman scattering was first observed in 1928 by C.V Raman and K.S. Krishnan [68]. This phenomenon results from elementary excitations in a material (in this work, we focus on vibrational states), and can, thus, reveal a substance's molecular fingerprint noninvasively – making Raman scattering a powerful tool for spectroscopy [69, 70]. Stimulated Raman scattering (SRS), on the other hand, is a four-wave nonlinear optical phenomenon in which a higher-frequency pump wave transfers some of its energy to a lower-frequency (Stokes) wave through the interaction of the pump with vibrations of the medium. The Stokes wave starts from spontaneous Raman scattering and is amplified as it gains energy from the pump wave while the pump wave is depleted. The energy difference between the pump and the Stokes waves is carried away by these vibrations, which are also known as optical phonons [4, 71]. The production of higher frequency (anti-Stokes) waves is also possible, however this is usually weak, particularly at low temperatures as as described by Maxwell-Boltzmann statistics [72]. Coherent anti-Stokes Raman spectroscopy (CARS) is a prime example of how SRS is used in spectroscopy [73]. Besides spectroscopy, SRS can also be used as the primary frequency conversion mechanism in nonlinear fibers lasers.

Liquid-filled fibers have gained prominence as noteworthy alternatives to solid-core fibers [74]. By comparison, solid-core fibers tend to exhibit greater dispersion and broader Raman gain spectra, while liquid-filled fibers offer a range of advantages vis-à-vis solid-core counterparts, including tunability by mixing liquids, higher Raman gain coefficients, and lower dispersion [75, 76]. The capability to modify the liquid type and concentration facilitates tailored adjustments of the Raman

gain spectrum and dispersion profile, thereby accommodating diverse application requirements. Furthermore, liquid-filled fibers can manifest heightened nonlinear coefficients when compared to silica glass, thereby necessitating reduced pump power levels and shorter fiber lengths for the attainment of significant Raman amplification.

Nonetheless, the utilization of liquid-filled fibers for nonlinear optics is not devoid of challenges. One of the biggest being the lack of data on Raman gain coefficients at specific pump wavelengths, such as 532 nm and 1064 nm, which are essential parameters for designing and optimizing devices leveraging SRS. The theory of SRS reveals that the Raman gain coefficient is proportional to the Raman scattering cross-section [71, 77, 78], which relates the irradiance of incident light to the intensity of the Raman scattered light for a given frequency shift and polarization state. The total cross-section as well as the differential scattering cross-section can be obtained from the spontaneous Raman spectrum. While the former requires careful calibration of the experimental setup, the latter can be straightforwardly measured with a referential technique and be used to calculate the gain coefficients of specific liquids of interest.

In this chapter, we present the calculated Raman gain measurements for eight solvents at 532 nm and 1064 nm. The solvents are benzene (C_6H_6), cyclohexane (C_6H_{12}), carbon disulfide (CS_2), toluene (C_7H_8), carbon tetrachloride (CCl_4), bromotrichloromethane ($CBrCl_3$), trichloroacetonitrile (CCl_3CN), and perfluorohexane (C_6F_{14}). We used a referential technique leveraging a 90° excitation geometry to obtain the polarized spontaneous Raman spectra of these liquids and the total differential Raman scattering cross-sections of their strongest scattered Stokes frequency. We also measured their depolarization ratios and linewidths using the same experimental setup. Using the experimental data reported throughout the chapter, along with the refractive indices and UV resonances that we reported in the previous chapter, we calculated the Raman gain coefficients of the solvents and compared them with the values found in the literature.

Theory

Classical Theory of Raman Scattering

In this section, we briefly go over the classical theory of Raman scattering following [79]. Before beginning, it is important to draw the distinction between light scattering processes and absorption. All light scattering processes are characterized by the fact that the energy of the incident light is not required to be equal to that of the energy corresponding to the difference between two energy levels of the material system. As will be pointed out throughout the chapter, however, the intensity of the scattered light is enhanced the closer the frequency of the incident light is to that of an electronic transition [80, 81].

Light, or electromagnetic radiation, originates from accelerating charges; and in this thesis, we limit our consideration of the origin of scattered radiation to oscillating electric dipole moments induced in molecules as a result of incident electromagnetic radiation. The intensity radiated by an oscillating electric dipole, I_s, induced in a molecule by an incident monochromatic electric field of frequency ω_1 (in s^{-1}) polarized along a direction making an angle θ with the axis of the dipole is given by [71, 79]:

$$I_s = \frac{\omega_s^4 |\vec{p}|^2 \sin^2 \theta}{32\pi^2 \varepsilon_0 c^3},\tag{3.1}$$

where ε_0 is the permittivity of free-space, c is the speed of light in free space, $\vec{p}$ is the dipole moment vector, and ω_s is dipole oscillation frequency, which is generally but not necessarily different from ω_1. Although it is convenient to use ω (in rad/s) in the theoretical treatments presented throughout this chapter, it is standard practice to use wavenumbers $\nu = 10^{-2} \omega/2\pi c$ (in cm^{-1}) in spectroscopy. Therefore, wavenumbers, ν, will arise throughout when relating theory with experiment.

Spontaneous Raman scattering is a linear process resulting from an induced dipole moment vector, $\vec{p}$, proportional to an oscillating electric field vector, $\vec{E}$:

$$\vec{p} = \bar{\alpha} \cdot \vec{E}, \tag{3.2}$$

where $\bar{\alpha}$ is the polarizability tensor that describes the tendency of a molecule to acquire a dipole moment. For Eq. 3.2, which is linear in $\vec{E}$, there can be three frequency components, one associated with Rayleigh scattering at ω_1, and two associated with Raman scattering at $\omega_1 \pm \omega_v$ where ω_v is a molecular vibrational frequency. We see, from Eq. 3.1, that $I_s \propto |\vec{p}|^2 \propto |\bar{\alpha} \cdot \vec{E}|^2$, and even if the electric field is perfectly aligned to one of the molecular axes, there can still be a dipole moment, and hence scattered radiation polarized, in a different direction due to the tensor nature of $\bar{\alpha}$ [82, 83].

In general, the polarizability tensor $\bar{\alpha}$ is a function of nuclear coordinates and, hence, of the molecular vibrational frequencies [79]. Raman scattering arises because the polarizability of the electrons to the electric field may, in some cases, depend upon the relative position of the nuclei in a given molecule [84]. Therefore, if the vibrations or rotations of a given molecule involve the displacement of the atomic nuclei, which changes the polarizability, then, as a consequence, one observes a shift in the frequency of the scattered light corresponding to the frequency of the nuclear motion [84]. When a molecule vibrates, the polarizability is modulated by each of its Raman-active normal vibrations, v. Taylor expanding $\bar{\alpha}$ in terms of the normal coordinates of vibration gives:

$$\bar{\alpha} = \bar{\alpha}_0 + \sum_v \left(\frac{\partial \bar{\alpha}}{\partial Q_v} \right)_0 Q_v + \cdots, \tag{3.3}$$

where $\bar{\alpha}_0$ is the value of $\bar{\alpha}$ at equilibrium, Q_v values are the normal coordinates of vibration associated with molecular vibrational frequencies ω_v and energy $\hbar\omega_v$, and the summation is over all normal coordinates. The subscript 0 in the derivative means that it is evaluated at equilibrium.

From quantum theory, we know that molecules are constantly in motion even if they are in their lowest vibrational energy state – this phenomenon is called the zero-point energy [72]. If we assume harmonic motion of the atomic nuclei, the time dependence of Q_v is given by:

$$Q_v = Q_{v_0} \cos(\omega_v t + \delta_v), \tag{3.4}$$

where Q_{v_0} is the amplitude of the nuclear motion and δ_v is a phase factor. Assuming an electric field vector of the form $\vec{E} = \vec{E}_0 \cos(\omega_1 t)$, inserting it into Eq. 3.2; and, inserting Eq. 3.4 into Eq. 3.3, and that into Eq. 3.2 yields:

$$\vec{p} = \bar{\alpha}_0 \cdot \vec{E}_0 \cos(\omega_1 t) + \frac{\bar{\alpha}'_v \cdot \vec{E}_0 Q_{k_0}}{2} \cos(\omega_1 t - \omega_v t - \delta_v) + \frac{\bar{\alpha}'_v \cdot \vec{E}_0 Q_{k_0}}{2} \cos(\omega_1 t + \omega_v t + \delta_v), \tag{3.5}$$

where $\bar{\alpha}'_v = (\partial \alpha / \partial Q_v)_0$ is called the Raman polarizability. The first term in Eq. 3.5 corresponds to Rayleigh scattering, the second term corresponds to Stokes Raman scattering, and the third term to anti-Stokes Raman scattering, respectively.

Looking back at Eq. 3.1 in connection with Eq. 3.5, this classical treatment provides a useful qualitative picture of the mechanisms behind Raman scattering. While Rayleigh scattering arises from an electric dipole oscillating at ω_1, Raman scattering arises from an electric dipole oscillating at $\omega_1 \pm \omega_v$; where we can think of the Stokes and anti-Stokes frequencies as being produced when a dipole oscillating at ω_1 is modulated by the molecule at frequency ω_v [79]. Also, it is evident that for any of the scattering processes to occur, their corresponding polarizabilities must be nonzero. Rayleigh scattering will always have nonzero components due to all molecules being polarizable to some extent. However, for the Raman polarizability to be nonzero, it must have a nonzero gradient with respect to the normal coordinate of vibration at the equilibrium position [79].

The total differential Raman scattering cross-section (TDRSC), $d\sigma/d\Omega$, is a constant of proportionality that relates the power of the incident light, P_0, to the power of the Raman scattered light, P_s, into a given solid angle [85–87]:

$$P_s = \left[\int_{\Omega_c} \frac{d\sigma}{d\Omega} d\Omega \right] P_0 NL, \tag{3.6}$$

where the integral is over the solid angle of collection Ω_c, N is the number density of scatterers, and L is the length from which scattered light is collected. Here, "total" means $d\sigma/d\Omega$ is obtained by integrating over the linewidth of the Raman line:

$$\frac{d\sigma}{d\Omega} = \int_v \frac{d\sigma}{d\Omega dv} dv, \tag{3.7}$$

and power arises from integrating the intensities of the incident and Raman scattered light over their linewidths:

$$P = \int_v I(v) dv. \tag{3.8}$$

In Eq. 3.7, $d\sigma/d\Omega dv$ is the peak differential scattering cross-section. Assuming a Lorentzian line-shape and constant Raman dispersion, i.e., assuming the intensity or power of the Raman scattered light as independent of frequency, Eq. 3.7 can be expressed as [86, 88]:

$$\frac{2}{\pi \Delta v} \frac{d\sigma}{d\Omega} = \frac{d\sigma}{d\Omega dv}, \tag{3.9}$$

where Δv is the linewidth of the Raman line. Integrating $d\sigma/d\Omega$ over all space, 4π Sr, gives the total Raman scattering cross-section [79, 86]:

$$\sigma = \int_{4\pi} \frac{d\sigma}{d\Omega} d\Omega. \qquad (3.10)$$

It has been shown experimentally that the spatial distribution of the intensity of Raman scattered light in a direction perpendicular, that is 90°, to the direction of the exciting laser beam is [86]:

$$I(\theta) = A + B\sin^2(\theta), \qquad (3.11)$$

where θ is the angle between the observation plane and and the exciting laser's polarization. The TDRSC of this 90°collection geometry is approximately [85]:

$$\Omega_c \frac{d\sigma}{d\Omega} \approx \int_{\Omega_c} \frac{d\sigma}{d\Omega} d\Omega. \qquad (3.12)$$

Then, combining Eq. 3.12 and Eq. 3.6 yields:

$$\frac{d\sigma}{d\Omega} = \frac{P_s}{P_0 N L \Omega_c}, \qquad (3.13)$$

where the solid angle of collection is given by $\Omega_c = hw/D^2 n^2$ – where h and w are the height and width, respectively, of the entrance slit to a spectrometer, D is the distance between the laser beam and the spectrometer entrance slit, and n is the refractive index of the scattering sample [86].

In terms of Placzek's polarizability theory, applicable away from electronic resonances, i.e., where the Raman polarizability theory is valid, for linearly-polarized light incident on a system of ran-

domly oriented molecules, the TDRSC can be expressed as [87, 89–91]:

$$\frac{d\sigma}{d\Omega} = \frac{16\pi^4}{45} \frac{(\nu_1 - \nu_v)^4}{1 - \exp(-2\pi\hbar c\nu_v/kT)} \frac{\hbar}{4\pi c\nu} g_v (45\alpha'^2 + 7\gamma'^2), \qquad (3.14)$$

where ν_1 and ν_v are wavenumbers corresponding to the exciting laser and Raman vibrational fre-
quency shift, respectively, g_v is the Raman line's degree of degeneracy, and α' and γ' are the
average isotropic and anisotropic parts of the Raman polarizability tensor associated with the νth
normal coordinate (molecular vibration), respectively – both of which are wavelength independent.
Note the only source of dispersion in Eq. 3.14 being $(\nu_1 - \nu_v)^4$ as in Eq. 3.1. And, the present
form of Eq. 3.14 applies to observations made in the direction perpendicular to the exciting laser
beam and its polarization [90–92], as Eq. 3.13.

The polarization of light scattered by a molecule may not be entirely along the same direction as
the exciting laser's polarization due to the tensor nature of the Raman polarizability. The ratio of
the intensity of light scattered along the same direction as the exciting laser's polarization, $I_{s,\parallel}$, to
the intensity of light scattered along the orthogonal direction, $I_{s,\perp}$, is given by [79, 82, 90, 93]:

$$\rho = \frac{I_{s,\perp}}{I_{s,\parallel}} = \frac{3\gamma'^2}{45\alpha'^2 + 4\gamma'^2}, \qquad (3.15)$$

where ρ is known as the depolarization ratio, $I_{s,\perp} \propto 3\gamma'^2$, and $I_{s,\parallel} \propto 45\alpha'^2 + 4\gamma'^2$. When using a
polarizer when measuring the scattered intensity gives:

$$\frac{d\sigma}{d\Omega} = (1 + \rho) \left(\frac{d\sigma}{d\Omega} \right)_{\parallel}, \qquad (3.16)$$

where $(d\sigma/d\Omega)_{\parallel}$ is the polarized TDRSC; its relationship to the orthogonal component is given
by $\rho(d\sigma/d\Omega)_{\parallel} = (d\sigma/d\Omega)_{\perp}$.

In SRS, the Stokes lines produced by spontaneous Raman scattering grow exponentially from quantum noise according to [87, 94, 95]:

$$I_s(l) = I_s(0)e^{g_R l I_0},$$ (3.17)

where $I_s(l)$ is the intensity of the stimulated Stokes emission, $I_s(0)$ is the intensity of the spontaneous Stokes emission, I_0 is the intensity of the pump laser, and l is the length of the amplifying medium. The Raman gain coefficient, g_R, is related to the total cross-section by [94]:

$$g_R = \frac{\sigma n}{c\hbar\omega_1},$$ (3.18)

where $n \approx n_s \approx n_0$ is the refractive index and ω_1 is the pump frequency. Plugging in the total cross-section:

$$\sigma = \frac{8\pi^2 \hbar \omega_1 \omega_s N}{cm\Delta\omega\omega_v n^3} \left(\frac{\partial\alpha}{\partial Q_v}\right)_0^2,$$ (3.19)

where ω_s is the Stokes frequency, m is the effective mass of the Raman mode, and ω_v is the Raman mode's frequency $\omega_v = \omega_1 - \omega_s$, into Eq. 3.18 yields:

$$g_R = \frac{8\pi^2 \omega_s N}{n^2 c^2 m\Delta\omega\omega_0} \left(\frac{\partial\alpha}{\partial Q_v}\right)_0^2.$$ (3.20)

The value of $(\partial\alpha/\partial Q_v)_0$ is needed to calculate g_R. Its relationship to the experimentally obtainable TDRSC is given by [94]:

$$\frac{d\sigma}{d\Omega} = \frac{\omega_s^4}{c^4} \left(\frac{\partial\alpha}{\partial Q_v}\right)_0^2 Q_v^2.$$ (3.21)

If we consider the energy of the harmonic oscillator to be the same in both the classical and the quantum theory, $Q_v^2 = \hbar/2m\omega_v$. Therefore:

$$\frac{d\sigma}{d\Omega} = \frac{\omega_s^4 \hbar}{2m\omega_v c^4} \left(\frac{\partial \alpha}{\partial Q_v}\right)_0^2. \tag{3.22}$$

Substituting this expression into the Eq. 3.20 yields the Raman gain coefficient in terms of the TDRSC:

$$g_R = \frac{16\pi^2 c^2 N}{\hbar \omega_s^3 n^2 \Delta\omega} \frac{d\sigma}{d\Omega} = \frac{8\pi c N}{\hbar \omega_s^3 n^2 \Delta\nu} \frac{d\sigma}{d\Omega}, \tag{3.23}$$

where $\Delta\omega = 2\pi c \Delta\nu$ is the full-width-half-max (FWHM) intensity of the spontaneous Raman line; note that $\Delta\nu$ is in wavenumbers (cm^{-1}). From its relationship to the TDRSC, the gain coefficient exhibits the same polarization dependence; where $g_{R,U} = (1+\rho)^{-1} g_{R,\parallel}$ and $\rho g_{R,\parallel} = g_{R,\perp}$.

Experiment

In the steady state regime, e.g., when using continuous-wave and nanosecond lasers, the spontaneous Raman lines most easily stimulated are those having high peak differential scattering cross-sections and narrow linewidths. However, when the pulse duration is of the same order as the lifetimes of the molecules in their vibrationally excited states, the stimulated Raman process becomes transient and the exponential gain coefficient is reduced [90, 96]. Since narrow linewidth Raman lines become more transient than broader linewidth transitions at pico- and sub-picosecond laser pulse excitation, the Raman lines having the greatest stimulated gain coefficient may no longer be those with the narrow spontaneous Raman linwewidths. Here, we focus on the steady state regime, which for the liquids we are investigating, occurs at pulse durations much greater than the Raman dephasing time [97]; the longest dephasing time, in our case, being that of CS2 of $\tau = 1/2\pi c \Delta\nu \approx 11$ ps. In our experiments and analysis, special emphasis will be given to the

strongest Raman lines of the spontaneous spectrum, measured from ~200 cm^{-1} to ~1200 cm^{-1}; which, with nanosecond or longer pulse excitation, would experience the highest gain.

To calculate the Raman gain coefficient of the eight solvents, we used the technique shown in Fig. 3.1 for measuring their spontaneous Raman intensities. With this well-known technique, we determined the TDRSC, Stokes frequency shift, depolarization ratio, and linewidth of their strongest Raman line – all of which are the necessary experimental parameters to be plugged into Eq. 3.23.
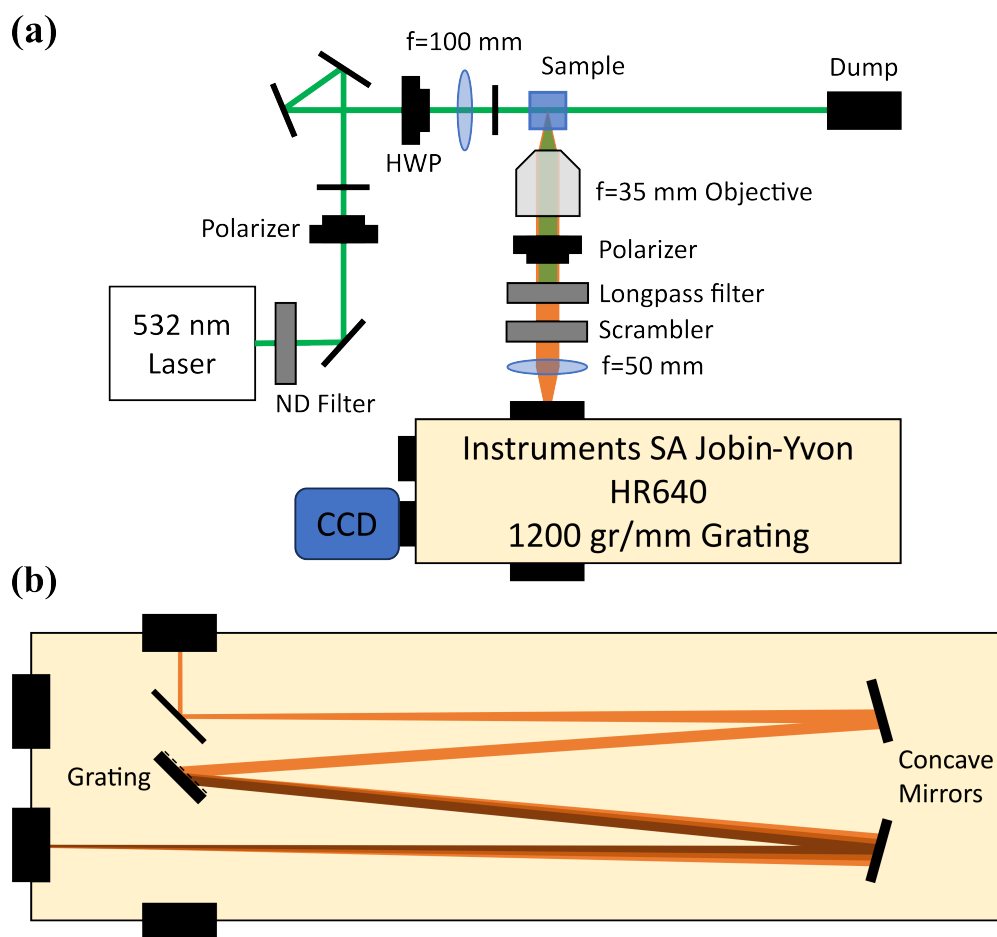
Figure 3.1: (a) Experiment setup for measuring spontaneous Raman scattering from a liquid sample. (b) Path light takes within the spectrometer.

As shown in Fig. 3.1, polarized Stokes Raman spectra were measured with an Instruments SA Jobin-Yvon HR640 single-grating spectrometer equipped with a Horiba SynapsePlus thinned back-illuminated charge-coupled device (CCD) cooled to -89.95 °C and a home-built attachment flange. The excitation source was a narrow linewidth, < 1 MHz FWHM, continuous-wave, $\lambda = 532$ nm, $> 100 : 1$ vertically polarized Cobolt 06-DPL laser from Hubner Photonics; we thank Dr. Kyu Young Han for letting us borrow the laser. A neutral density (ND) filter was used after the laser for alignment at low powers, and a Glan-Taylor polarizer was used to ensure vertical polarization. Then, a half-wave plate was used to ensure the polarization is set to vertical before going into the sample, and an $f = 100$ mm lens was used to focus the beam into the sample. The system utilized a 90° excitation geometry where the light scattered orthogonal to the direction of propagation of the input beam was collected, following Eq. 3.13. Typical input powers were ~30 mW (measured after the focusing lens), and we did not observe any photo-induced effects before and after measurements. The samples under investigation were purchased from Sigma-Aldrich and used without further purification. We used single-chamber 10 ± 0.01 mm pathlength cuvettes from Starna made of Spectrosil quartz. All cuvettes were tested against each other by filling them with the same liquid, e.g., carbon tetrachloride, and signals obtained with each, for both vertical and horizontal polarization, were identical.

Scattered light from the sample was collected with a Mitutoyo $f = 35$ mm microscope objective that was properly placed to ensure the light following it was collimated. A prism polarizer was used after the microscope objective to individually select the vertical and horizontally-polarized Raman scattered signals from the sample. The polarized light was passed through a Semrock RazorEdge longpass filter to remove the Rayleigh scattered component, and a polarization scrambler was used to mitigate the impact of the grating's polarization sensitivity. Finally, an $f = 50$ mm lens was used to focus the spectrum onto the slits, shown in Fig. 3.2(a), which were opened to 2 μm. We used a 1200 groove/mm blazed grating, Fig. 3.2(b), and the CCD dimensions were 2048×512 with pixel

sizes of 13.5×13.5 μm. With this combination, we had a ~0.5 cm^{-1} resolution; however, we had to characterize the system's impulse response to extract true linewidths via the convolution of two Lorentzians.
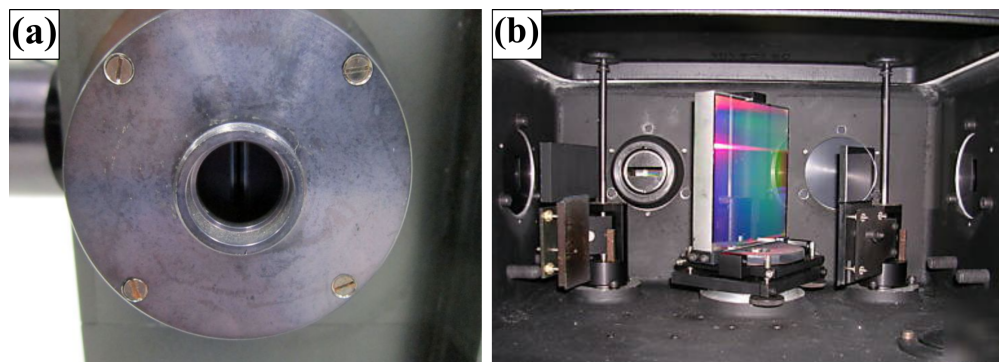
Figure 3.2: (a) Entrance slits to the spectrometer, set to 2 μm during the experiments. (b) View of the inside of the spectrometer. Light comes in through the vertical opening on the right side, is reflected from the mirror to the right of the grating, is collimated with by a concave mirror (not shown) and sent to the grating, the diffracted signal reflects from the grating to another concave mirror (not shown), and is focused to the opening of the CCD, which is the horizontal opening to the back-left side of the grating.

Depolarization ratios, ρ following Eq. 3.15, were measured by adjusting the polarizer after the sample. Vertically polarized light scattered from the vertically polarized input was labeled (VV), and horizontally polarized light scattered from the vertically polarized input was labeled (VH). Intensity measurements were made by setting the polarizer to either VV or VH, and used the CCD software to integrate the signal for 10 seconds, averaged three times, for a total capture time of 30 seconds per polarization.

Following the procedure outlined by Schneebeli et al. [98], we obtained the TDRSC of the different solvents by using a reference standard liquid, identical excitation geometry, and collection optics, which allowed us to determine specific experimental variables that may prove challenging to measure. In our case, the use of a referential technique alleviates the need for determining the

solid angle of collection, Ω_c, of our setup. It is worth mentioning that the method of Colles et al. [90], where unknown liquids are mixed with a known reference, is another good alternative to obtain the TDRSC without having to account for Ω_c as long as the known sample's TDRSC is known. However, this technique may not work for all combinations of liquids since intermolecular forces may not always be neglected.

In a similar manner to Schneebeli et al. [98], we have chosen to utilize a referential method to determine the TDRSC from straightforwardly obtained experimental parameters. Taking the ratio of the Eq. 3.13 for an unknown sample to a known reference yields:

$$\left(\frac{d\sigma}{d\Omega}\right)_{sam} = \left(\frac{d\sigma}{d\Omega}\right)_{ref} \cdot \frac{P^s_{sam}}{P^s_{ref}} \cdot \frac{P^0_{ref}}{P^0_{sam}} \cdot \frac{N_{ref}}{N_{sam}} \cdot \frac{L_{ref}}{L_{sam}} \cdot \frac{n^2_{sam}}{n^2_{ref}}, \qquad (3.24)$$

where *sam* and *ref* denote the sample and reference, respectively, $P^s = \int_\nu I^s(\nu)d\nu$ is the Raman scattered power determined from integrating the Raman line intensity, P^0 is the power of the laser used to excite the sample, N is the number density of molecules, and L is the pathlength of the laser through the sample. Correction for refractive index variations across samples is taken into consideration through the n^2_{sam}/n^2_{ref} term, which results from the ratio of Ω_c as defined below Eq. 3.13. The relative standard deviation error of this technique is estimated to be $\pm$ 25%, calculated using standard of error propagation, with its main contribution coming from the error in $(d\sigma/d\Omega)_{ref}$ [98].

For the present method to yield proper results, a well-characterized reference standard is needed. Throughout the years, several authors have published results on the TDRSC of the 992 cm^{-1} breathing mode of benzene [86–88, 92, 98–104]. In the studies we were able to find, however, excitation wavelengths other than 532 nm were used. Therefore, we extrapolated the value of the cross-section of the 992 cm^{-1} mode of benzene by gathering as much information as possible on its measurements at different wavelengths and fitting a curve to all the data using the frequency de-

pendence of the TDRSC.

Expressing $d\sigma/d\Omega$ in terms of the Kramers-Heisenberg equation [86]:

$$\frac{d\sigma}{d\Omega} = \frac{4\pi^2 q^4 v_s^4}{\varepsilon_0^2 \hbar^2 c^2} \left| \sum_\gamma \frac{\langle s|x_s|\gamma\rangle \langle \gamma|x_1|1\rangle}{(v_\gamma - v_1)} + \frac{\langle s|x_s|\gamma\rangle \langle \gamma|x_1|1\rangle}{(v_\gamma + v_1)} \right|^2, \tag{3.25}$$

reveals additional terms affecting the dispersion of the Raman cross-section. In Eq. 3.25, q is the electronic charge, $v_s = v_1 - v_v$ is the frequency (in wavenumbers, cm^{-1}) of the Raman scattered light, γ represents the γth electronic excited state of the material, and braketed terms are the elements of the scattering matrix. Taking Eq. 3.25 and Van Vleck's expansion [105] as a starting point, Albrecht developed an approach to the formulation of the Raman effect that contains explicit reference to excited vibronic states and is valid under resonance conditions when properly formulated [106]. With Albrecht's approach, if the frequencies characterizing two virtual electronic states, v_γ and v_η, and the frequency of the incident light is v_1, the following relationship is obtained with near-resonance conditions [91, 106]:

$$\frac{d\sigma}{d\Omega} \propto I^R \propto (v_1 - v_v)^4 \left[\frac{(v_\gamma v_\eta + v_1^2)^2}{(v_\gamma^2 - v_1^2)^2 (v_\eta^2 - v_1^2)^2} \right]. \tag{3.26}$$

However, when $v_\eta \to v_\gamma$, i.e., they are closely lying vibronically mixing electronic states, the above equation reduces to [91, 106]:

$$\frac{d\sigma}{d\Omega} \propto I^R \propto (v_1 - v_v)^4 \left[\frac{(v_\gamma^2 + v_1^2)^2}{(v_\gamma^2 - v_1^2)^4} \right], \tag{3.27}$$

which is identical in form to the equation resulting from the semiclassical theory of Shorygin [91, 106]. When the frequency of the exciting radiation is much lower than the frequencies associated with the virtual transitions, but much higher than the Raman frequency shift, then the intensity is simply $d\sigma/d\Omega \propto I^R \propto (v_1 - v_v)^4$.

43

Since at 532 nm we are not too close and not too far from resonance enhancement, we found Eq. 3.27 to work best in this case. With Eq. 3.27, we obtained the Raman dispersion of the 992 cm^{-1} vibrational mode of benzene shown in Fig. 3.3. For better visualization, we used a double log plot where the vertical axis is the cross-section in $\times 10^{-33}$ m^2/(molecule Sr) and the vertical axis is in kilo-Kaisers (kK), which are $\times 1000$ cm^{-1}. We chose an electronic resonance wavelength of $1/\nu_\gamma = \lambda_\gamma = 144$ nm, which gave a good fit. From this fit, the TDRSC value we selected at 532 nm for Eq. 3.24 was $(d\sigma/d\Omega)_{ref} = 2.58 \times 10^{-33}$ m^2/(molecule Sr). When the spontaneous Stokes scattering of a particular sample's line at 532 nm is determined with the referential technique, this value is dispersion-corrected to 1064 nm by using Eq. 3.27 with the $\lambda_{UV} = \lambda_\gamma$ Sellmeier coefficients given in the last chapter. All TDRSC values at 532 nm and 1064 nm are then plugged into Eq. 3.23 with the linewidths we measured. All results are presented in the following section.
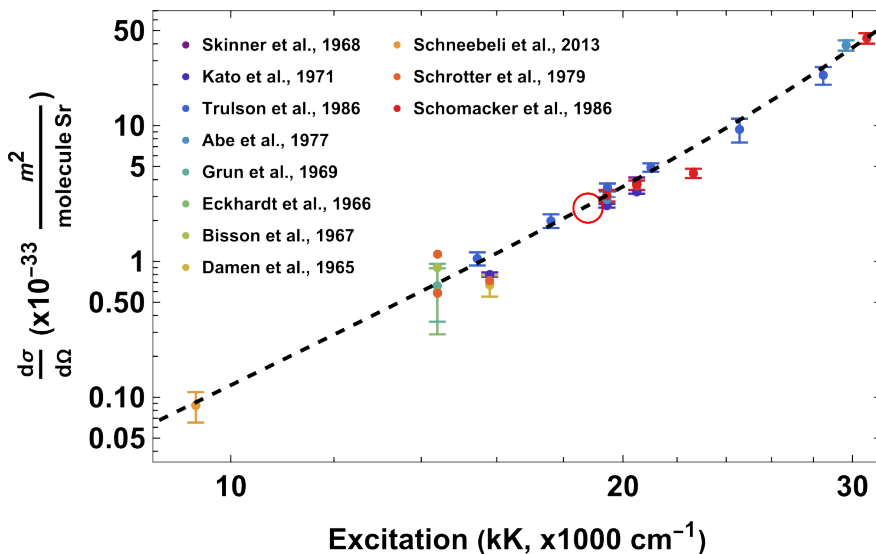
Figure 3.3: Raman dispersion of the 992 cm^{-1} line of benzene. Colored points and error bars are values found across the literature reported at different excitation wavenumbers. The black-dashed trace is a fit of Eq. 3.27 using a UV resonance wavelength of $1/\nu_\gamma = \lambda_\gamma = 144$ nm, and the empty red circle represents the value of $d\sigma/d\Omega$ we selected at 532 nm.

Results

Following the procedure outlined in the previous section, we first measured the spontaneous Raman intensities at both VV and VH polarizations for the different liquids of interest: C6H6 (the reference), C6H12, CS2, C7H8, CCl4, CBrCl3, CCl3CN, and C6F14, as shown in Figs. 3.4-3.11. The frequency shift and depolarization ratio corresponding to the most intense Raman lines, measured from ~200 to ~1200 cm^{-1}, is given in the description of the figures. In the original spectra, the horizontal axis of Figs. 3.4-3.11 was in pixels. We measured and used the Raman spectrum of naphthalene (C10H8) as a standard of calibration for the axis [107]. Using linear interpolation, we assigned wavenumber values to each pixel, hence the slight differences between our frequency shifts and those reported in the literature.
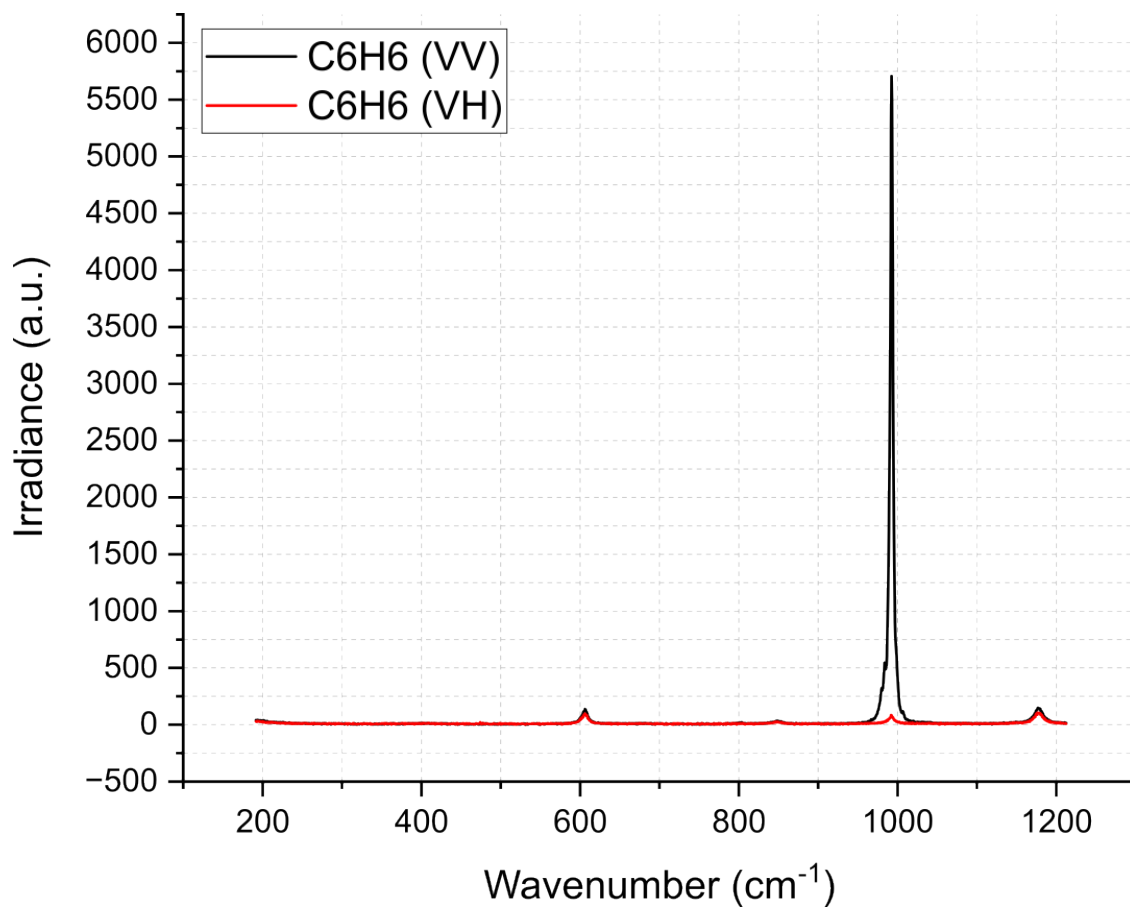
Figure 3.4: Polarized spectrum of C6H6. The frequency shift of the strongest Raman line is $v_v = 992.5$ cm^{-1} with a depolarization ratio $\rho = 0.01$.
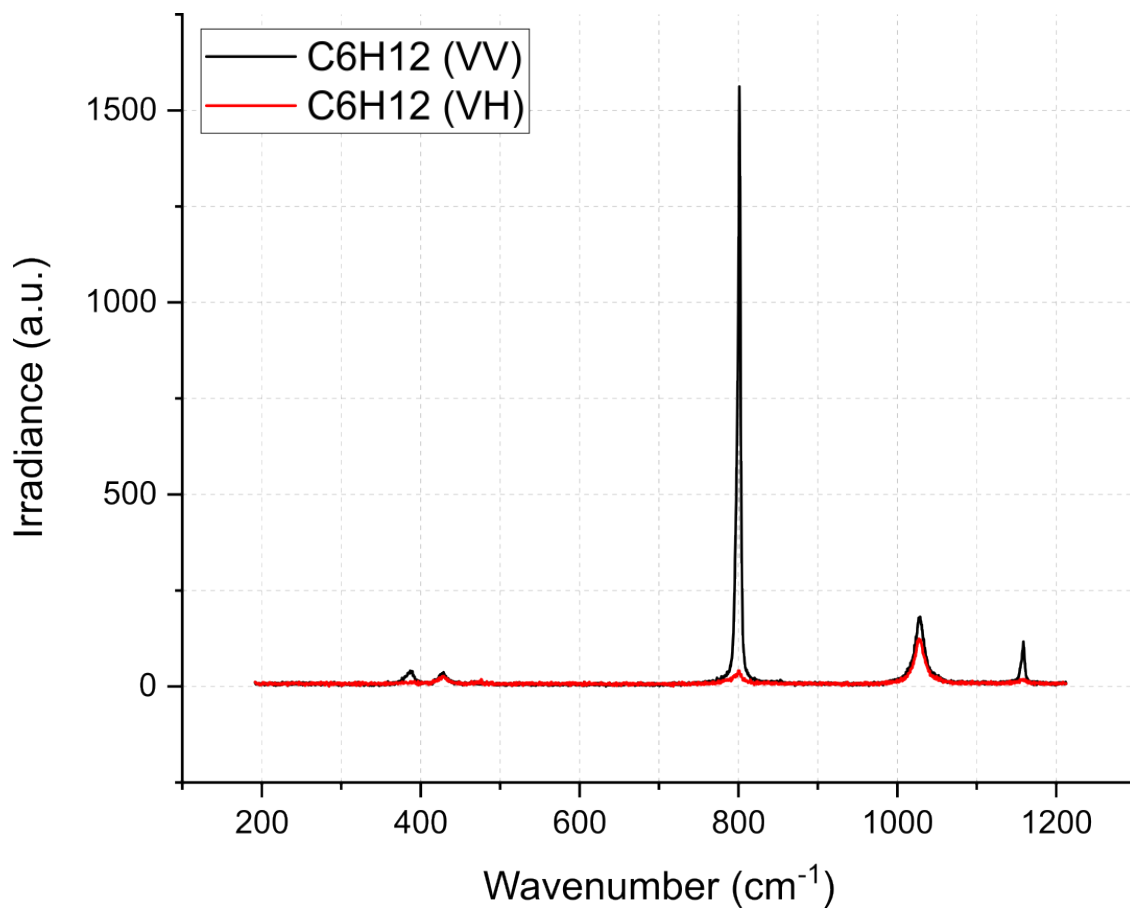
Figure 3.5: Polarized spectrum of C6H12. The frequency shift of the strongest Raman line is $\nu_v = 801.3$ cm^{-1} with a depolarization ratio $\rho = 0.02$.
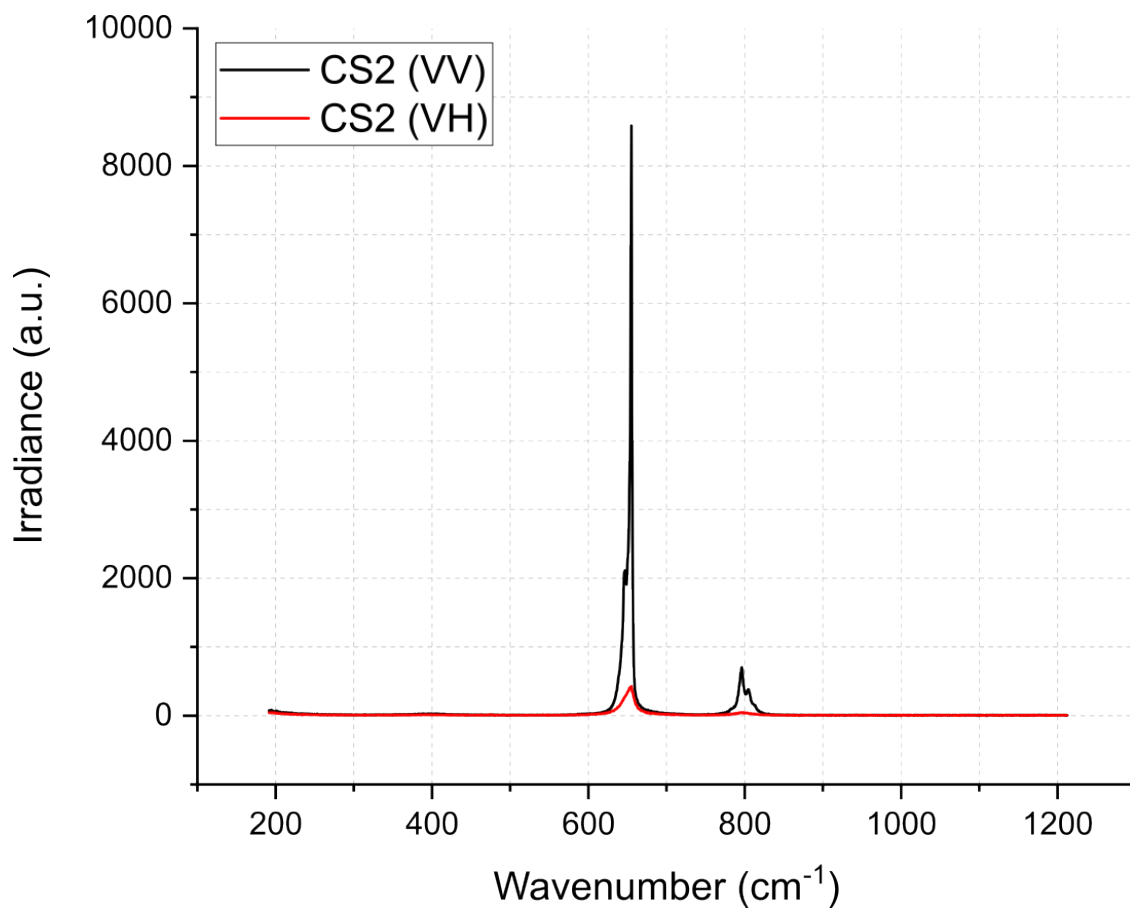
Figure 3.6: Polarized spectrum of CS2. The frequency shift of the strongest Raman line is $\nu_v = 655.1$ cm^{-1} with a depolarization ratio $\rho = 0.05$.
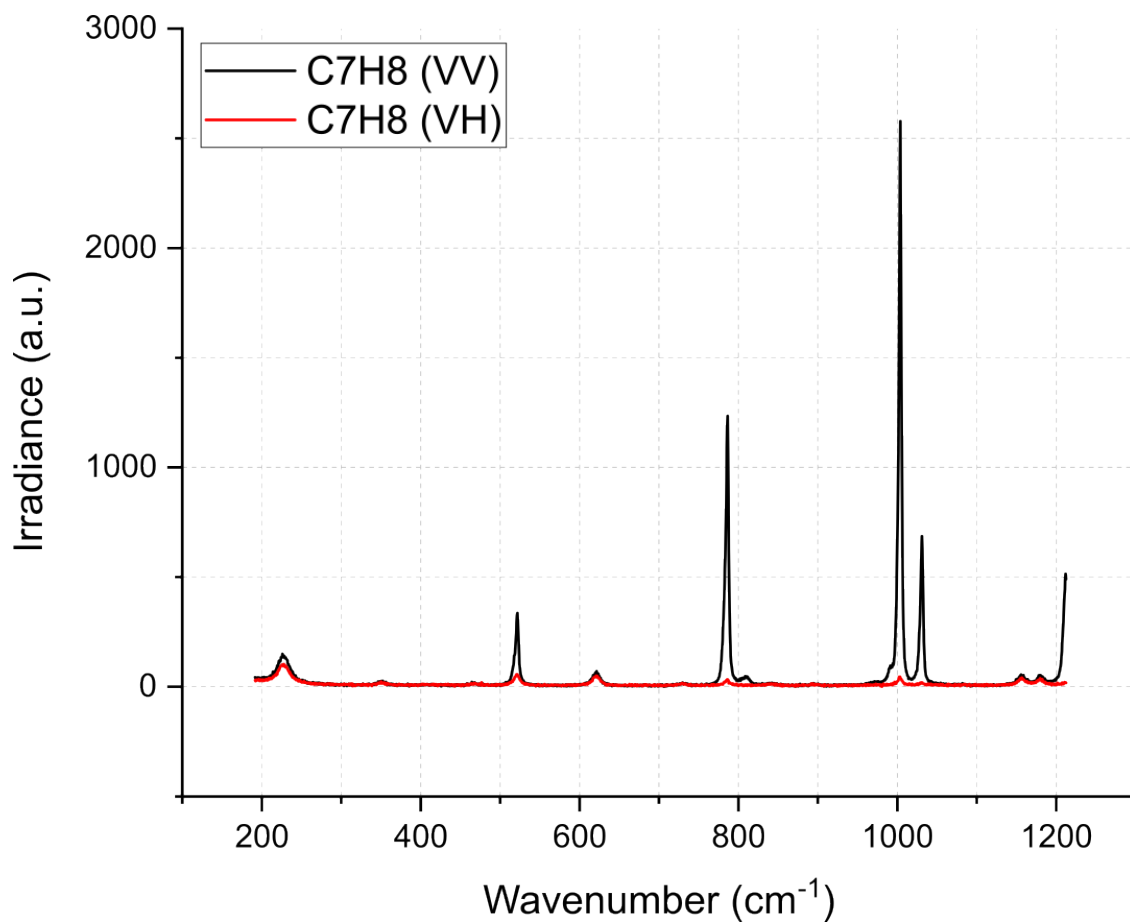
Figure 3.7: Polarized spectrum of C7H8. The frequency shift of the strongest Raman line is $\nu_v = 1003.9$ cm^{-1} with a depolarization ratio $\rho = 0.02$.
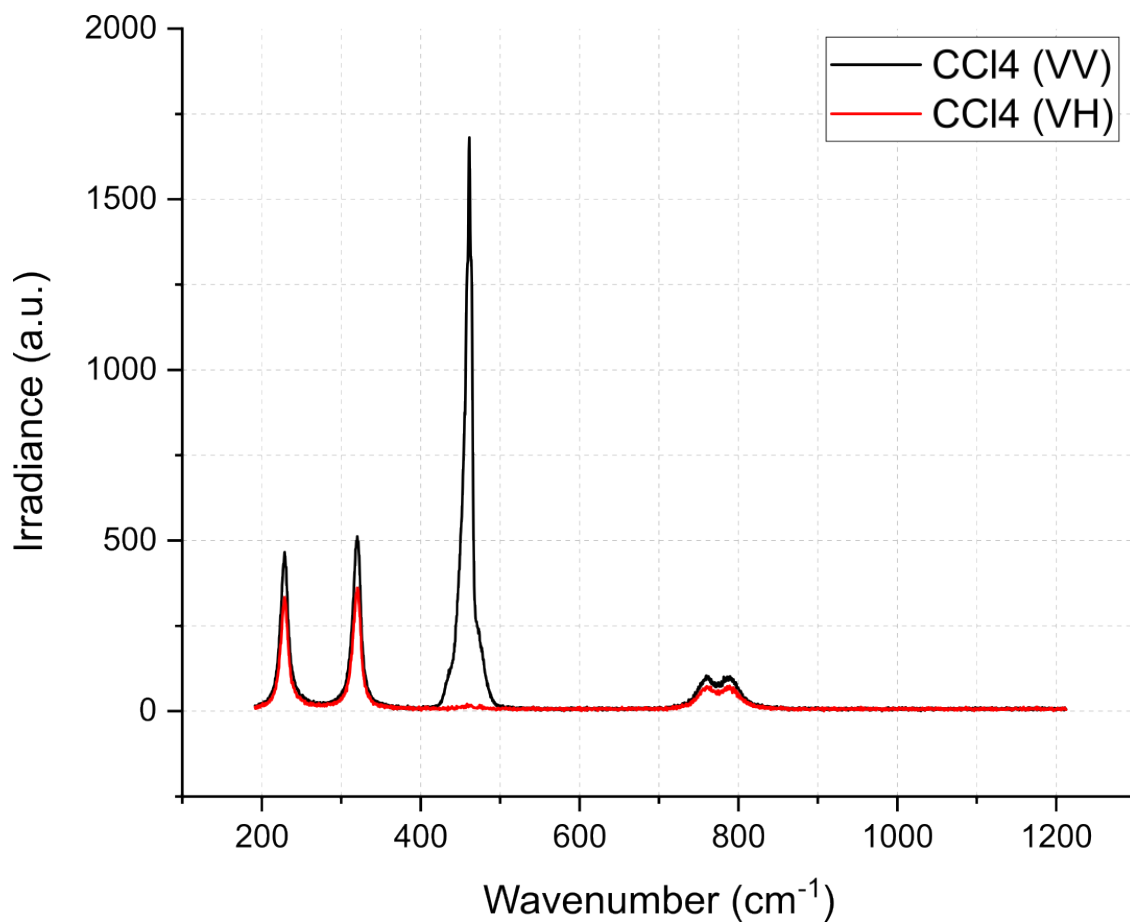
Figure 3.8: Polarized spectrum of CCl4. The frequency shift of the strongest Raman line is $v_v = 461.5$ cm^{-1} with a depolarization ratio $\rho = 0.01$.
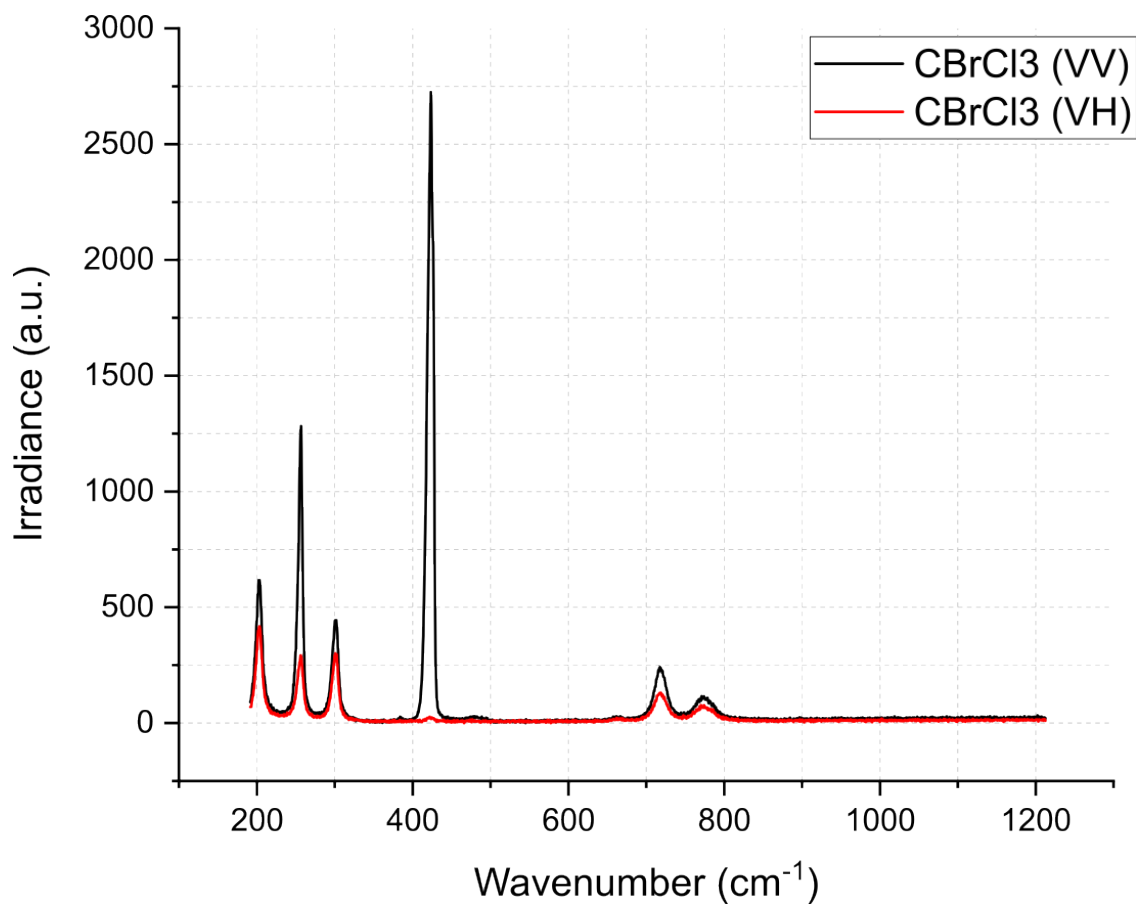
Figure 3.9: Polarized spectrum of CBrCl3. The frequency shift of the strongest Raman line is $v_v = 423.4$ cm^{-1} with a depolarization ratio $\rho = 0.009$.
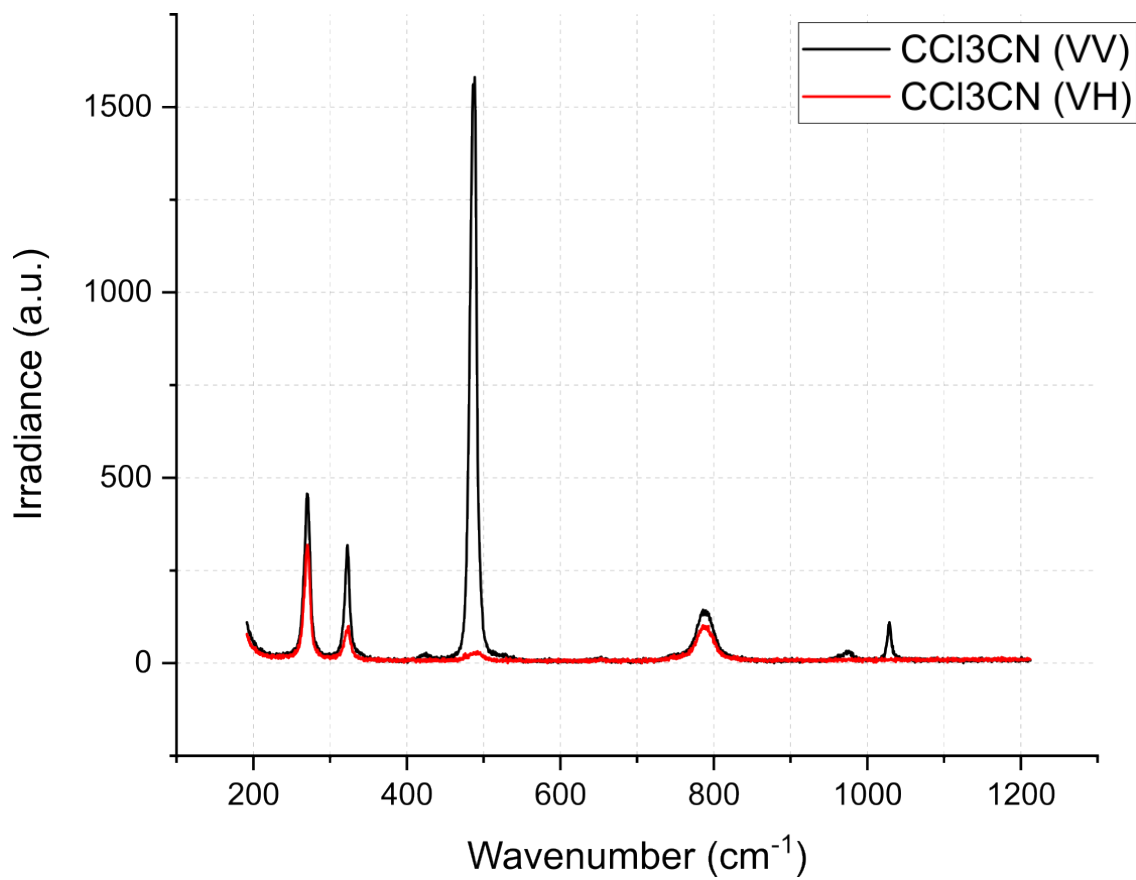
Figure 3.10: Polarized spectrum of CCl3CN. The frequency shift of the strongest Raman line is $\nu_v = 488.4$ cm^{-1} with a depolarization ratio $\rho = 0.02$.
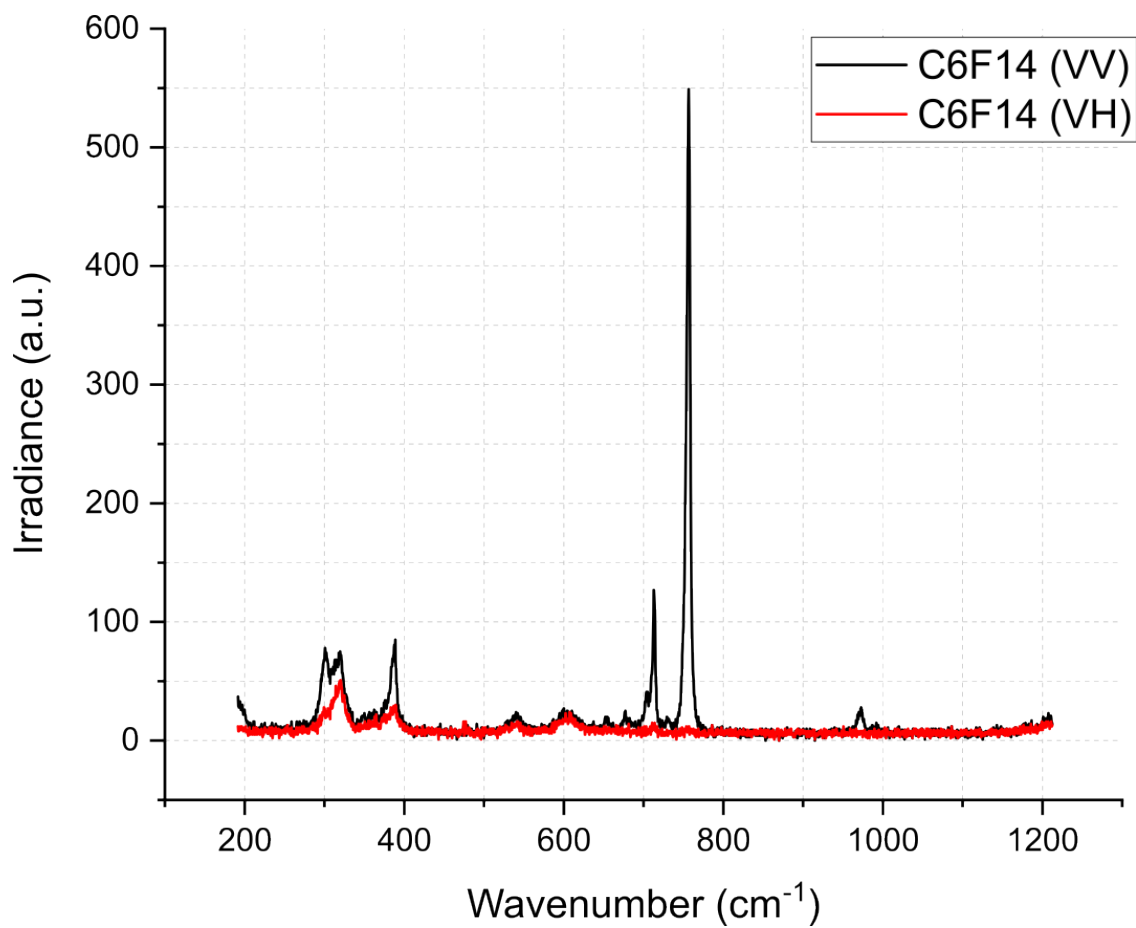
Figure 3.11: Polarized spectrum of C6F14. The frequency shift of the strongest Raman line is $v_v = 756.7$ cm^{-1} with a depolarization ratio $\rho = 0.02$.

To ensure that we are doing the referential technique correctly, we computed the TDRSC of well-known solvents such as C6H12, CS2, and CCl4. In Figs. 3.12-3.14, we compare our measured TDRSCs (red star marker with error bars) against other values reported in literature [87, 92, 95, 98–100]. The dashed-black trace is Eq. 3.27 fitted to the data using the electronic resonances, $\lambda_{UV} = \lambda_\gamma$, reported in the previous chapter.
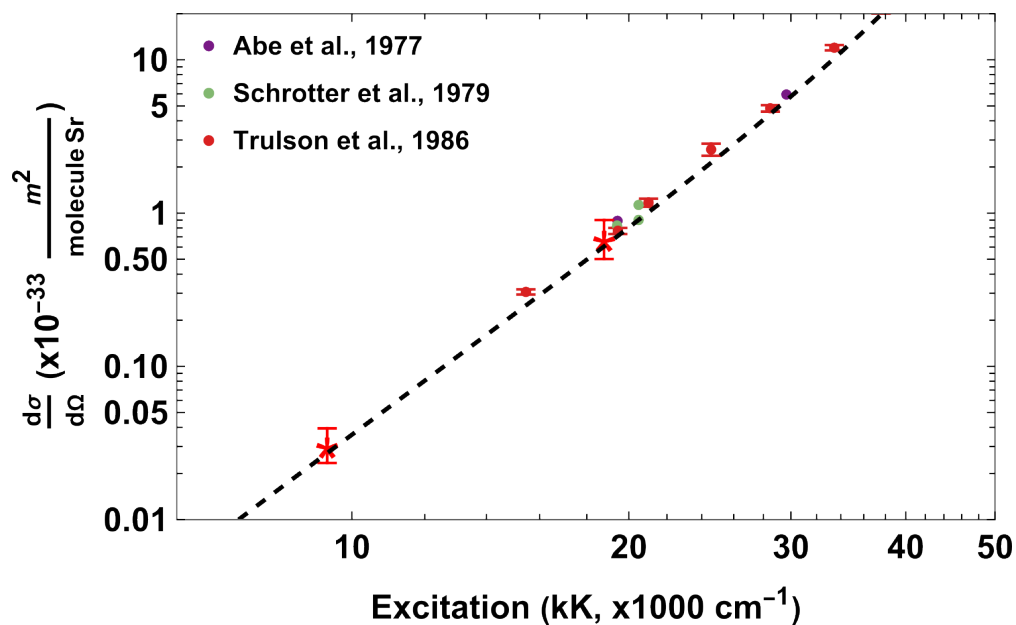
Figure 3.12: Raman dispersion of the 801 cm^{-1} line of cyclohexane. Colored points and error bars are values found across the literature reported at different excitation wavenumbers. The black-dashed trace is a fit of Eq. 3.27 using a UV resonance wavelength of $\lambda_{UV} = 97.1$ nm, and the red star represents the value of $d\sigma/d\Omega$ we measured at 532 nm and dispersion corrected to 1064 nm.
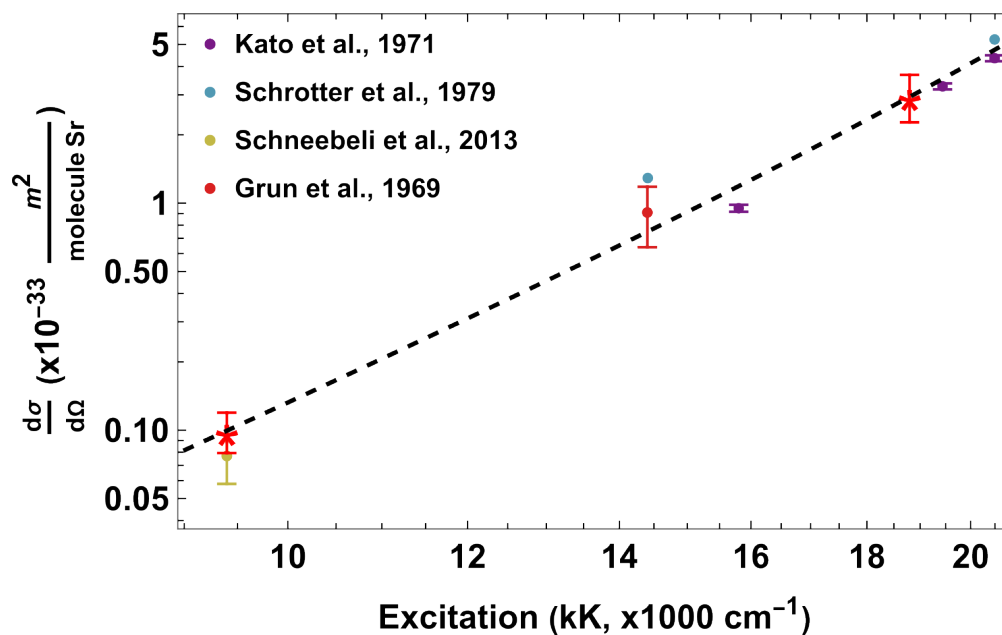
Figure 3.13: Raman dispersion of the 656 cm^{-1} line of carbon disulfide (referred to as 655 cm^{-1} in this work). Colored points and error bars are values found across the literature reported at different excitation wavenumbers. The black-dashed trace is a fit of Eq. 3.27 using a UV resonance wavelength of $\lambda_{UV} = 169$ nm, and the red star represents the value of $d\sigma/d\Omega$ we measured at 532 nm and dispersion corrected to 1064 nm.
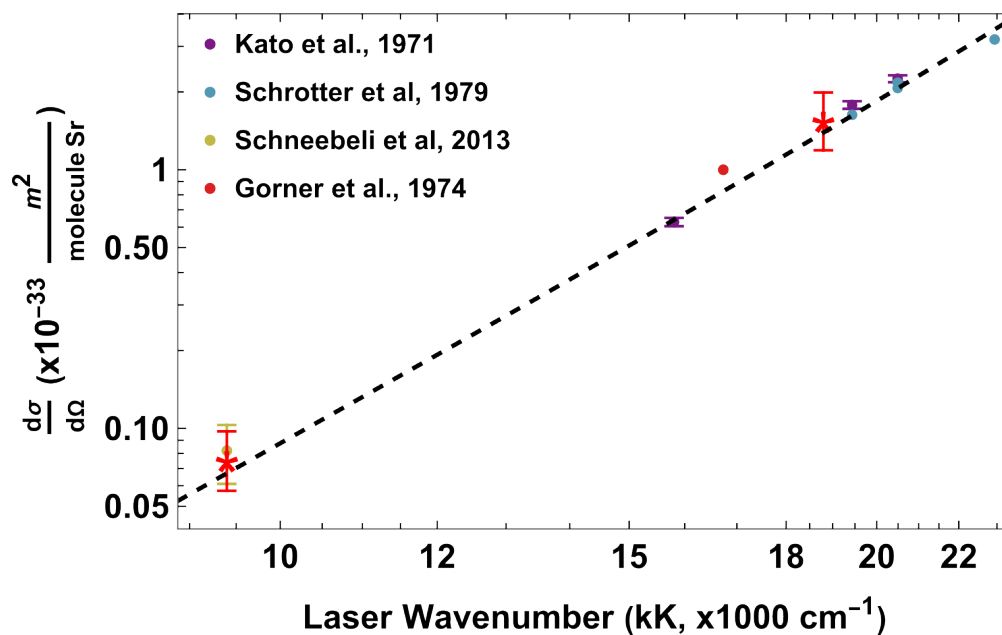
Figure 3.14: Raman dispersion of the 459 cm^{-1} line of carbon disulfide (referred to as 461 cm^{-1} in this work). Colored points and error bars are values found across the literature reported at different excitation wavenumbers. The black-dashed trace is a fit of Eq. 3.27 using a UV resonance wavelength of $\lambda_{UV} = 99.6$ nm, and the red star represents the value of $d\sigma/d\Omega$ we measured at 532 nm and dispersion corrected to 1064 nm.

To obtain the TDRSCs, we calculated the total Raman powers, P^s, of the strongest Raman lines by numerically integrating them with OriginPro. For most lines, we performed the integration from the ends of the Lorentzian 'tails.' However, for CCl4 we did not include the contribution of the asymmetric tails and for CS2 we included the neighboring lower frequency line (648.8 cm^{-1}) that overlaps with the 655 cm^{-1} line. For the number density of molecules, N, of each solvent, we used the formula $N = $ density $\times$ Avogadro's number/molar mass. For the refractive index, we assumed $n_0 \approx n_s$. For the laser power and pathlength ratios, $P^0_{ref}/P^0_{sam} \approx L_{ref}/L_{sam} \approx 1$, since, for the duration of the experiment, the power fluctuated by less than we could measure and the pathlengths of the cuvettes were identical (within $\pm$ 0.01 mm). Given the good agreement of our measured TDRSCs with the expected dispersion from those reported in literature, shown in Figs. 3.12-3.14, we proceeded to calculate the rest. All TDRSCs and the parameters used for calculating them are listed in Table 3.1.

Table 3.1: Total Differential Raman Scattering Cross-Section (m^2/(molecule Sr)) of Solvents Measured in this Work

Solvent	v_v cm^{-1}	ρ	P^s a.u.	$N \times 10^{27}$ m^3	n	$\frac{d\sigma}{d\Omega} \times 10^{-33}$ at 532 nm	$\frac{d\sigma}{d\Omega} \times 10^{-35}$ at 1064 nm*
C6H6 (ref)	992.5	0.01	34626.91	6.77	1.50	2.58	9.17
C6H12	801.3	0.02	8524.135	5.57	1.43	0.701	3.14
CS2	655.1	0.05	49670.6	9.97	1.63	2.97	10.1
CCl4	461.5	0.01	20746.86	6.22	1.46	1.59	7.77
C7H8	1003.9	0.02	12839.395	5.67	1.50	1.14	4.23
CBrCl3	423.4	0.009	26658.03	5.83	1.51	2.34	10.6
CCl3CN	488.4	0.02	19333.62	6.09	1.44	1.48	7.00
C6F14	756.7	0.02	3791.445	2.99	1.25	0.444	2.06

*TDRSC values at 1064 nm are dispersion-corrected from 532 nm by using Eq. 3.27.

We ensured that all results were repeatable by measuring the Raman spectra and TDRSCs several times over several days and with different slit-widths. By changing the slitwidth, we noticed that not only did the signal registered by the CCD become stronger when opening them up more, but the Raman lines became broader. This occurs because the narrower the slit width is, the narrower

the slit image will be at the detector's focal plane, and a narrower slit image corresponds to a higher spectral resolution. With this improvement in resolution, we were able to better resolve the true FWHM of the Raman lines, but were still limited by the width of the CCD's pixels. Still, we found that using slit-widths of 2 μm was the best compromise between resolution and signal-to-noise ratio.

The last key parameter we needed for calculating the gain coefficient was the linewidth, as shown in Eq. 3.23. From the Raman spectra shown in Figs. 3.4-3.11, only the apparent linewidth can be extracted. Thinking of our spectrometer as an imaging system, the spectrum we measure is in reality the convolution of the true Raman spectrum with the system's impulse response (or point-spread function). To find our system's impulse response, i.e. the convolution of a delta function line with the system's response, we measured the Rayleigh scattered light from a sample and the narrowest Raman line of the liquids; which was CS2's with a FWHM value of 0.5 ± 0.02 cm^{-1} [108]. A Gaussian with a FWHM of ~2.1 cm^{-1} best fitted the Rayleigh line. Unfortunately, the fitting of Voigt functions obtained by convolving the Lorentzian shape of the Raman lines with the Gaussian impulse response did not produce satisfactory results. We then attempted to deconvolute the 655 cm^{-1} line of CS2 using a combination of Lorentzians, as illustrated in Fig. 3.15. This resulted in a Lorentzian fit to the 655 cm^{-1} line with a FWHM of ~2 cm^{-1}, which defined the impulse response – the narrowest feature our spectrometer could resolve. All operations were performed using OriginPro.

By assuming that the impulse response of our system is Lorentzian, we were able to simplify our analysis significantly. It is known that the convolution of two Lorentzians results in a new Lorentzian with a FWHM equal to the sum of the individual Lorentzian widths [109]:

$$L_a(\omega) = L_r(\omega) * L_t(\omega) = \frac{\Delta v_r + \Delta v_t}{\pi} \cdot \frac{1}{\omega^2 + (\Delta v_r + \Delta v_t)^2}, \tag{3.28}$$
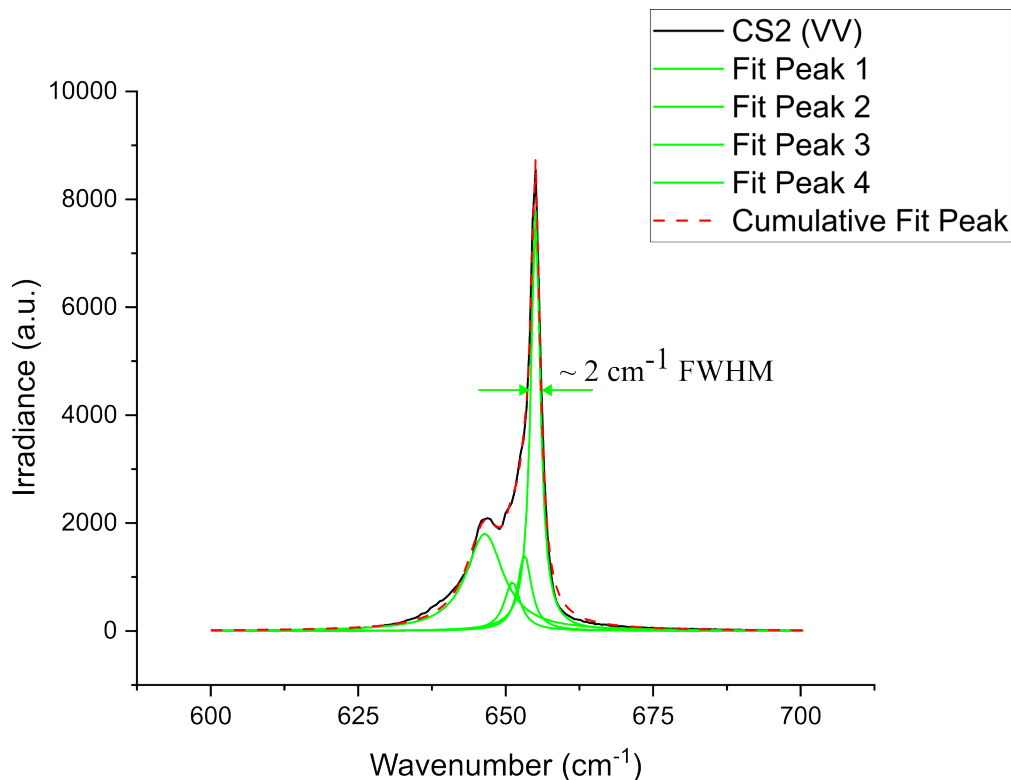
Figure 3.15: Deconvolution of CS2 spectrum for characterizing the system's impulse response. Fitted peak centers are at 646.5 cm^{-1}, 651.1cm^{-1}, 653.2cm^{-1}, and 655.1 cm^{-1}. From these, the FWHM of the system's impulse response was ~2 cm^{-1}.

where L_a, L_r, and L_t are apparent, response, and true Lorentzian functions, respectively, and Δv_a, Δv_r and Δv_t are their corresponding linewidths. Using this relation, we can calculate the linewidths of our liquids as follows: $\Delta v_t = \Delta v_a - \Delta v_r = \Delta v_a - 2$ cm^{-1}, where Δv_t is the true linewidth of the Raman lines. It is important to note that without this procedure, the linewidths we obtain directly from the spectrometer, shown in Figs. 3.4-3.6, are the apparent linewidths, Δv_a. Assuming that all the Raman lines of interest in this work are Lorentzians, we can repeat this procedure for all of our liquids to get their true linewidths. Using this method, we list all of the linewidths obtained for each of the liquids in Table 3.2 and compare them with values found across the literature. We found our values to be in good agreement with those reported in the literature.

Table 3.2: Linewidths of Strongest Raman lines of Solvents Measured in this Work

Solvent	$\Delta\nu$ cm^{-1} in this work	$\Delta\nu$ cm^{-1} in the literature
C6H6	2.1	2.15 ± 0.15 [108], 2.3 ± 0.05 [86], 2.1 [98], 2.24 [90], 2.1 ± 0.1 [110], 3.1 [111]
C6H12	2.0	1.6 ± 0.1 [112], 2.12 [90]
CS2	0.50	0.50 ± 0.02 [108], 1.4 [86], 1.2 [98]
CCl4	8.5	7 [97], 8.1 [98]
C7H8	1.6	1.94 ± 0.07 [108]
CBrCl3	7.4	
CCl3CN	7.9	
C6F14	3.3	

Finally, we calculate the Raman gain coefficients by plugging in the values from Tables 3.1 and 3.2 into Eq. 3.23, which yields the results shown in Table 3.3. The error associated with the reported gain coefficients is estimated to be $\pm30\%$ using the present technique [98]. We compare our calculated values to those found in the literature and indicate their measured or calculated wavelength in parenthesis. Our calculated values are in agreement with those reported in the literature. It is important to note that the frequency dependence of the gain coefficient is quite different from that of the TDRSC. To elaborate, $d\sigma/d\Omega \propto (\nu_1 - \nu_v)^4$ and from Eq. 3.23 $g_R \propto (\nu_1 - \nu_v)^{-3}$ before accounting for the frequency dependence of the cross-section. Combining both terms gives $g_R \propto (\nu_1 - \nu_v)$, which implies that we expect the gain coefficient to increase linearly with Stokes frequency, as long as we are not near electronic resonances [113].

Table 3.3: Calculated Raman gain coefficients (cm/GW) of Solvents Measured in this Work

Solvent	Calculated g_R at 532 nm	Extrapolated g_R at 1064 nm	g_R in the literature
C6H6	7.04	2.38	5.48(532 nm) [114], 2.8(694 nm) [115], 0.63(1550 nm) [98]
C6H12	1.76	0.723	
CS2	40.1	12.1	12-75(694 nm) [94], 24(694 nm) [115], 10(694 nm) [116], 1.3-3(1550 nm) [98]
CCl4	0.954	0.401	1.3(~590 nm) [20], 2.4(1100 nm) [20], 0.16-0.15(1550 nm) [98]
C7H8	3.43	1.21	3.47(532 nm) [114], 1.2(694 nm) [71]
CBrCl3	1.40	0.544	
CCl3CN	0.960	0.395	
C6F14	0.471	0.199	

CHAPTER 4: CONCLUSION AND FUTURE WORKS

This chapter concludes the work done on two projects: the measurement of refractive index of different liquids using the Rayleigh interferometry technique and the calculation of Raman gain coefficients of different liquids using a referential technique to measure their total differential Raman cross-section.

Refractive Index Measurements Using Rayleigh Interferometry

In Chapter 2, we presented a novel interferometric technique for measuring the refractive index of liquids at seven different wavelengths. We presented equations describing the relative phase between a beam that passed through a reference with known index and a sample of unknown refractive index. By fitting these equations to experimental data that was obtained by tracking the movement of interference peaks as a function of incident angle, we were able to obtain the refractive index of 26 different solvents. The movement of the peaks of the interference pattern were the only important information needed during the experiment. This technique was simple to set up, worked well even in cases where liquid absorption was high (poor fringe contrast), and worked best for our laboratories.

Depending on the wavelength, two different cameras and a pinhole detector were used to record the fringes. For wavelengths ranging 543 nm to 1064 nm, we used the Coherent beam profiler. At 1550 nm, we used an InGaAs camera. And, at 1970 nm, we used the pinhole detector to scan across the fringes. The latter case shows that this technique is not limited by the availability of cameras, but it does take more time to record the data and care should be taken to keep the temperature as steady as possible for the duration of the experiment.

We then fitted one to two-term Sellmeier equations to our measured indices to provide dispersion information for the liquids. The choice of using Sellmeier equations stems from being near absorption bands in the infrared, and the Sellmeier equation is based on a physical model of dispersion [117]. From our fits, we obtained UV resonance values, λ_{UV}, that were subsequently used in the spontaneous Raman experiments.

Some potential future improvements and interesting phenomena to investigate are as follows. In terms of improvements, one the sources of error we had to account for when doing the experiment was the vertical displacement of the beams not being centered on the focusing lens. Fortunately, this effect was negligible for most liquids we measured due to the long focal length of the lens used after the cuvette to create the interference pattern. Care should be taken when using focal lengths comparable to the horizontal spacing and vertical displacement of the beams, and the use of a cylindrical lens would simplify the analysis as we would only have to account for its focal length and vertical position of the beams. In terms of interesting phenomena to investigate further, although not reported here, we performed refractive index measurements of a mixture of CCl_4 and C_2Cl_4. Our results suggest that the refractive indices or susceptibilities of the liquids we analyzed do not follow a simple linear combination. This observation may prompt the use of an equation such as the Lorentz-Lorenz equation for a binary mixture of liquids [114]. We also noticed that the refractive index of the mixture was higher than that of the individual liquids, indicating that molecular interactions, such as London dispersion forces [118], or other effects could be at play.

Stimulated Raman Gain Measurements from Spontaneous Raman Scattering

In Chapter 3, we used a well-known technique using a 90°excitation geometry to measure the total differential Raman cross-section of eight selected solvents and calculate their Raman gain coefficients at pump wavelengths of interest, such as 532 nm and 1064 nm. Using benzene as

the reference standard liquid, identical excitation geometry, and collection optics for all liquids, alleviated the need to account for specific experimental variables that may have been challenging to measure. We compared this technique against scattering cross-section data available in the literature for several of the solvents, and we found good agreement. In addition, we explored the dispersion of the spontaneous Raman effect, and found it useful to include the electronic transition we obtained from the Sellmeier fits given in Chapter 2. Using the same technique, setup, and spectrometer, we were able to obtain accurate depolarization ratios and the linewidths of the Raman lines. Throughout the chapter, we listed all experimental parameters used to calculate the Raman gain coefficients of the different liquids at 532 nm and 1064 nm, and found agreement with values available in the literature. We also provided a brief discussion on the frequency dependence of the gain coefficient derived from its dependence on the cross-section.

As a potential next step, or general consideration, we suggest verifying the calculated gain coefficients by using a different experimental technique. One possible option is to use hollow silica fibers filled with liquids as Raman amplifiers, and measure the output power as a function of input power and fiber length. This technique would directly yield the gain coefficient of the liquids at the pump frequency without relying on a standard reference. Given the availability of a 785 nm laser in our laboratories, we are considering repeating these experiments at that wavelength. Given its proximity to 1064 nm and it being further from resonance enhancement, it would provide a good middle ground for verifying the accuracy of our extrapolations and the $(v - v_i)^4$ correction factor.

As a future direction, we are interested in investigating the Raman spectra of different samples of silica glass, which are used in many cases as standard materials and in a myriad of applications in optics. We aim to calculate the nuclear contribution to the nonlinear refractive index, n_2, from their Raman spectra and compare results with Z-scan measurements. We expect to find variations in n_2 depending on the type and composition of silica glass.

REFERENCES

[1] G. Stegeman and R. Stegeman, *Nonlinear Optics: Phenomena, Materials and Devices* (Wiley Series in Pure and Applied Optics). Wiley, 2012, ISBN: 9781118072721. [Online]. Available: `https://books.google.com/books?id=W124BQAAQBAJ`.

[2] J. M. Dudley, G. Genty, and S. Coen, "Supercontinuum generation in photonic crystal fiber," *Reviews of modern physics*, vol. 78, no. 4, p. 1135, 2006.

[3] O. Aso, M. Tadakuma, and S. Namiki, "Four-wave mixing in optical fibers and its applications," *dEp*, vol. 1, no. 2, 1999.

[4] D. Cotter *et al.*, "Nonlinear optics for high-speed digital information processing," *Science*, vol. 286, no. 5444, pp. 1523–1528, 1999.

[5] M. Takeoka, R.-B. Jin, and M. Sasaki, "Full analysis of multi-photon pair effects in spontaneous parametric down conversion based photonic quantum information processing," *New Journal of Physics*, vol. 17, no. 4, p. 043030, 2015.

[6] P. Van Loock, "Optical hybrid approaches to quantum information," *Laser & Photonics Reviews*, vol. 5, no. 2, pp. 167–200, 2011.

[7] A. M. Wallace *et al.*, "Design and evaluation of multispectral lidar for the recovery of arboreal parameters," *IEEE Transactions on Geoscience and Remote Sensing*, vol. 52, no. 8, pp. 4942–4954, 2013.

[8] E. Ip *et al.*, "Qpsk transmission over free-space link at 3.8 μm using coherent detection with wavelength conversion," in *Proc. 34th Eur. Conf. Opt. Commun*, Citeseer, 2008, pp. 1–2.

[9] F. Vidal and A. Tadjeddine, "Sum-frequency generation spectroscopy of interfaces," *Reports on Progress in Physics*, vol. 68, no. 5, p. 1095, 2005.

[10] P. Kukura, D. W. McCamant, and R. A. Mathies, "Femtosecond stimulated Raman spectroscopy," *Annu. Rev. Phys. Chem.*, vol. 58, pp. 461–488, 2007.

[11] P. Berto, E. R. Andresen, and H. Rigneault, "Background-free stimulated Raman spectroscopy and microscopy," *Physical review letters*, vol. 112, no. 5, p. 053 905, 2014.

[12] P. F. Moulton, A. Dergachev, Y. Isyanova, B. Pati, and G. Rines, "Recent advances in solid state lasers and nonlinear optics for remote sensing," *Lidar Remote Sensing for Industry and Environment Monitoring III*, vol. 4893, pp. 193–202, 2003.

[13] C. B. Marble and V. V. Yakovlev, "Biomedical optics applications of advanced lasers and nonlinear optics," *Journal of Biomedical Optics*, vol. 25, no. 4, pp. 040 902–040 902, 2020.

[14] B. T. Kuhlmey, B. J. Eggleton, and D. K. Wu, "Fluid-filled solid-core photonic bandgap fibers," *Journal of Lightwave Technology*, vol. 27, no. 11, pp. 1617–1630, 2009.

[15] C. Lopez-Zelaya, C. K. Keyser, M. Raab, P. Hemmer, W. Larson, and T. L. Courtney, "Numerical exploration of organic liquid-filled fibers," in *2022 IEEE Research and Applications of Photonics in Defense Conference (RAPID)*, IEEE, 2022, pp. 1–2.

[16] D. Dobrakowski *et al.*, "Antiresonant fibers with single-and double-ring capillaries for optofluidic applications," *Optics Express*, vol. 28, no. 22, pp. 32 483–32 498, 2020.

[17] K. Kieu, L. Schneebeli, R. Norwood, and N. Peyghambarian, "Integrated liquid-core optical fibers for ultra-efficient nonlinear liquid photonics," *Optics express*, vol. 20, no. 7, pp. 8148–8154, 2012.

[18] N. Perron, M. Chemnitz, B. Fischer, S. Junaid, M. Schmidt, and R. Morandotti, "All-optical digital processing in carbon disulfide liquid-core optical fiber," in *2023 Conference on Lasers and Electro-Optics (CLEO)*, IEEE, 2023, pp. 1–2.

[19] W. Huang, S. Junaid, J. Hofmann, H. Schneidewind, and M. A. Schmidt, "Ultrafast supercontinuum generation in halomethane-filled liquid-core fibers," *Optics Letters*, vol. 48, no. 20, pp. 5411–5414, 2023.

[20] A. Chraplyvy and T. Bridges, "Infrared generation by means of multiple-order stimulated Raman scattering in ccl 4-and cbrcl 3-filled hollow silica fibers," *Optics letters*, vol. 6, no. 12, pp. 632–633, 1981.

[21] C. K. Keyser, M. E. Raab, P. Hemmer, C. Lopez-Zelaya, T. L. Courtney, and J. Timler, "Charting a course to efficient difference frequency generation in molecular-engineered liquid-core fiber," *Optics Express*, vol. 31, no. 10, pp. 15 722–15 735, 2023.

[22] J. Campo, F. Desmet, W. Wenseleers, and E. Goovaerts, "Highly sensitive setup for tunable wavelength hyper-rayleigh scattering with parallel detection and calibration data for various solvents," *Optics Express*, vol. 17, no. 6, pp. 4587–4604, 2009.

[23] S. Junaid *et al.*, "Attenuation coefficients of selected organic and inorganic solvents in the mid-infrared spectral domain," *Optical Materials Express*, vol. 12, no. 4, pp. 1754–1763, 2022.

[24] F. M. Cox, A. Argyros, and M. C. J. Large, "Liquid-filled hollow core microstructured polymer optical fiber," *Opt. Express*, vol. 14, no. 9, pp. 4135–4140, May 2006. DOI: 10. 1364/OE.14.004135. [Online]. Available: https://opg.optica.org/oe/abstract. cfm?URI=oe-14-9-4135.

[25] Y. Zhu, X. Chen, Y. Xu, and Y. Xia, "Propagation properties of single-mode liquid-core optical fibers with subwavelength diameter," *J. Lightwave Technol.*, vol. 25, no. 10, pp. 3051–3056, Oct. 2007. [Online]. Available: https://opg.optica.org/jlt/abstract.cfm? URI=jlt-25-10-3051.

[26] R. Zhang, J. Teipel, X. Zhang, D. Nau, and H. Giessen, "Group velocity dispersion of tapered fibers immersed in different liquids," *Opt. Express*, vol. 12, no. 8, pp. 1700–1707, Apr. 2004. DOI: `10.1364/OPEX.12.001700`. [Online]. Available: `https://opg.optica.org/oe/abstract.cfm?URI=oe-12-8-1700`.

[27] M. Vieweg *et al.*, "Ultrafast nonlinear optofluidics in selectively liquid-filled photonic crystal fibers," *Opt. Express*, vol. 18, no. 24, pp. 25 232–25 240, Nov. 2010. DOI: `10.1364/OE.18.025232`. [Online]. Available: `https://opg.optica.org/oe/abstract.cfm?URI=oe-18-24-25232`.

[28] J. Bethge *et al.*, "Two-octave supercontinuum generation in a water-filled photonic crystal fiber," *Opt. Express*, vol. 18, no. 6, pp. 6230–6240, Mar. 2010. DOI: `10.1364/OE.18.006230`. [Online]. Available: `https://opg.optica.org/oe/abstract.cfm?URI=oe-18-6-6230`.

[29] K. Kieu, L. Schneebeli, R. A. Norwood, and N. Peyghambarian, "Integrated liquid-core optical fibers for ultra-efficient nonlinear liquid photonics," *Opt. Express*, vol. 20, no. 7, pp. 8148–8154, Mar. 2012. DOI: `10.1364/OE.20.008148`. [Online]. Available: `https://opg.optica.org/oe/abstract.cfm?URI=oe-20-7-8148`.

[30] M. Chemnitz *et al.*, "Hybrid soliton dynamics in liquid-core fibres," *Nature Communications*, vol. 8, no. 1, p. 42, 2017.

[31] J. Liu, H. Schroeder, S. L. Chin, R. Li, and Z. Xu, "Nonlinear propagation of fs laser pulses in liquids and evolution of supercontinuum generation," *Opt. Express*, vol. 13, no. 25, pp. 10 248–10 259, Dec. 2005. DOI: `10.1364/OPEX.13.010248`. [Online]. Available: `https://opg.optica.org/oe/abstract.cfm?URI=oe-13-25-10248`.

[32] L. Guyon *et al.*, "Control of lasing filament arrays in nonlinear liquid media," *Applied Physics B*, vol. 90, pp. 383–390, 2008.

[33] D. Psaltis, S. R. Quake, and C. Yang, "Developing optofluidic technology through the fusion of microfluidics and optics," *Nature*, vol. 442, no. 7101, pp. 381–386, 2006.

[34] C. Monat, P. Domachuk, and B. Eggleton, "Integrated optofluidics: A new river of light," *Nature Photonics*, vol. 1, no. 2, pp. 106–114, 2007.

[35] D. P. Shelton, "Nonlocal hyper-rayleigh scattering from liquid nitrobenzene," *The Journal of Chemical Physics*, vol. 132, no. 15, p. 154 506, 2010.

[36] B. Chandra and S. Bhaiya, "A simple, accurate alternative to the minimum deviation method of determining the refractive index of liquids," *American Journal of Physics*, vol. 51, no. 2, pp. 160–161, 1983.

[37] D. Jenkins, "Refractive indices of solutions," *Physics Education*, vol. 17, no. 2, p. 82, 1982.

[38] A. Zaidi, Y. Makdisi, K. Bhatia, and I. Abutahun, "Accurate method for the determination of the refractive index of liquids using a laser," *Review of Scientific Instruments*, vol. 60, no. 4, pp. 803–805, 1989.

[39] H. Hattori, H. Yamanaka, H. Kurniawan, S. Yokoi, and K. Kagawa, "Using minimum deviation of a secondary rainbow and its application to water analysis in a high-precision, refractive-index comparator for liquids," *Appl. Opt.*, vol. 36, no. 22, pp. 5552–5556, Aug. 1997. DOI: 10.1364/AO.36.005552. [Online]. Available: https://opg.optica.org/ao/abstract.cfm?URI=ao-36-22-5552.

[40] H. Hattori, H. Kakui, H. Kurniawan, and K. Kagawa, "Liquid refractometry by the rainbow method," *Appl. Opt.*, vol. 37, no. 19, pp. 4123–4129, Jul. 1998. DOI: 10.1364/AO.37.004123. [Online]. Available: https://opg.optica.org/ao/abstract.cfm?URI=ao-37-19-4123.

[41] K. Kuhler, E. L. Dereniak, and M. Buchanan, "Measurement of the index of refraction of the plastic Phenoxy PKFE," *Appl. Opt.*, vol. 30, no. 13, pp. 1711–1714, May 1991. DOI: 10.1364/AO.30.001711. [Online]. Available: https://opg.optica.org/ao/abstract.cfm?URI=ao-30-13-1711.

[42] S. Kedenburg, M. Vieweg, T. Gissibl, and H. Giessen, "Linear refractive index and absorption measurements of nonlinear optical liquids in the visible and near-infrared spectral region," *Opt. Mater. Express*, vol. 2, no. 11, pp. 1588–1611, Nov. 2012. DOI: 10.1364/OME.2.001588. [Online]. Available: https://opg.optica.org/ome/abstract.cfm?URI=ome-2-11-1588.

[43] J. E. Saunders, C. Sanders, H. Chen, and H.-P. Loock, "Refractive indices of common solvents and solutions at 1550 nm," *Appl. Opt.*, vol. 55, no. 4, pp. 947–953, Feb. 2016. DOI: 10.1364/AO.55.000947. [Online]. Available: https://opg.optica.org/ao/abstract.cfm?URI=ao-55-4-947.

[44] S. Nemoto, "Measurement of the refractive index of liquid using laser beam displacement," *Appl. Opt.*, vol. 31, no. 31, pp. 6690–6694, Nov. 1992. DOI: 10.1364/AO.31.006690. [Online]. Available: https://opg.optica.org/ao/abstract.cfm?URI=ao-31-31-6690.

[45] F. Docchio, S. Corini, M. Perini, and R. Gasana, "A simple and reliable system for measuring the refractive index of liquids using a position-sensitive detector," *IEEE Transactions on Instrumentation and Measurement*, vol. 44, no. 1, pp. 68–70, 1995. DOI: 10.1109/19.368101.

[46] D. P. Shelton, "Refractive index measured by laser beam displacement at $\lambda = 1064$ nm for solvents and deuterated solvents," *Appl. Opt.*, vol. 50, no. 21, pp. 4091–4098, Jul. 2011. DOI: 10.1364/AO.50.004091. [Online]. Available: https://opg.optica.org/ao/abstract.cfm?URI=ao-50-21-4091.

[47] X. Wu, M. Muntzeck, T. de Los Arcos, G. Grundmeier, R. Wilhelm, and T. Wagner, "Determination of the refractive indices of ionic liquids by ellipsometry, and their application as immersion liquids," *Applied Optics*, vol. 57, no. 31, pp. 9215–9222, 2018.

[48] J. Den Boer, G. Kroesen, and F. De Hoog, "Measurement of the complex refractive index of liquids in the infrared using spectroscopic attenuated total reflection ellipsometry: Correction for depolarization by scattering," *Applied optics*, vol. 34, no. 25, pp. 5708–5714, 1995.

[49] X. Li, C. Wang, L. Ma, and L. Liu, "Ellipsometry-transmission measurement of the complex refractive indices for a series of organic solvents in the 200–1700 nm spectral range," *Infrared Physics & Technology*, vol. 125, p. 104 313, 2022.

[50] T. L. Myers *et al.*, "Accurate measurement of the optical constants n and k for a series of 57 inorganic and organic liquids for optical modeling and detection," *Applied Spectroscopy*, vol. 72, no. 4, pp. 535–550, 2018.

[51] C. Gouveia, M. Zibaii, H. Latifi, M. J. Marques, J. M. Baptista, and P. A. Jorge, "High resolution temperature independent refractive index measurement using differential white light interferometry," *Sensors and Actuators B: Chemical*, vol. 188, pp. 1212–1217, 2013.

[52] C. Sainz, J. Calatroni, and G. Tribillon, "Refractometry of liquid samples with spectrally resolved white light interferometry," *Measurement Science and Technology*, vol. 1, no. 4, p. 356, 1990.

[53] A. Guerrero, C. Sainz, H. Perrin, R. Castell, and J. Calatroni, "Refractive index distribution measurements by means of spectrally-resolved white-light interferometry," *Optics & Laser Technology*, vol. 24, no. 6, pp. 333–339, 1992.

[54] S. Singh, "Refractive index measurement and its applications," *Physica Scripta*, vol. 65, no. 2, p. 167, 2002.

[55] H. El-Kashef, "The necessary requirements imposed on polar dielectric laser dye solvents," *Physica B: Condensed Matter*, vol. 279, no. 4, pp. 295–301, 2000.

[56] H. El-Kashef, "Study of the refractive properties of laser dye solvents: Toluene, carbon disulphide, chloroform, and benzene," *Optical Materials*, vol. 20, no. 2, pp. 81–86, 2002.

[57] S. De Nicola, P. Ferraro, A. Finizio, G. Pesce, and G. Pierattini, "Reflective grating interferometer for measuring the refractive index of transparent materials," *Optics Communications*, vol. 118, no. 5-6, pp. 491–494, 1995.

[58] P. Marteau, G. Montixi, J. Obriot, T. Bose, and J. St. Arnaud, "An accurate method for the refractive index measurements of liquids: Application of the kramers–kronig relation in the liquid phase," *Review of Scientific Instruments*, vol. 62, no. 1, pp. 42–46, 1991.

[59] H.-J. Chang, "First and third order susceptibility of organic molecules," 2022.

[60] K. Moutzouris, M. Papamichael, S. C. Betsis, I. Stavrakas, G. Hloupis, and D. Triantis, "Refractive, dispersive and thermo-optic properties of twelve organic solvents in the visible and near-infrared," *Applied Physics B*, vol. 116, pp. 617–622, 2014.

[61] A. Samoc, M. Samoc, B. Luther-Davies, R. Stockmann, H. Tillmann, and H.-H. Hoerhold, "Third-order optical nonlinearities of poly (arylamino-phenylenevinylene) studied with femtosecond pulses," in *Optoelectronics, Materials, and Devices for Communications*, SPIE, vol. 4580, 2001, pp. 347–356.

[62] I. Z. Kozma, P. Krok, and E. Riedle, "Direct measurement of the group-velocity mismatch and derivation of the refractive-index dispersion for a variety of solvents in the ultraviolet," *J. Opt. Soc. Am. B*, vol. 22, no. 7, pp. 1479–1485, Jul. 2005. DOI: 10.1364/JOSAB.22.001479. [Online]. Available: https://opg.optica.org/josab/abstract.cfm?URI=josab-22-7-1479.

[63] J. E. Bertie, Z. Lan, R. N. Jones, and Y. Apelblat, "Infrared intensities of liquids XVIII: Accurate optical constants and molar absorption coefficients between 6500 and 800 cm- 1 of dichloromethane at 25° c, from spectra recorded in several laboratories," *Applied spectroscopy*, vol. 49, no. 6, pp. 840–851, 1995.

[64] S. Ghosal, J. L. Ebert, and S. A. Self, "The infrared refractive indices of CHBr3, CCl4 and CS2," *Infrared Physics*, vol. 34, no. 6, pp. 621–628, 1993.

[65] P. Linstorm, "Nist chemistry webbook, nist standard reference database number 69," *J. Phys. Chem. Ref. Data, Monograph*, vol. 9, pp. 1–1951, 1998.

[66] *AIST: Spectral database for organic compounds, SDBS*, `https://sdbs.db.aist.go.jp/sdbs/cgi-bin/direct_frame_top.cgi`, Accessed: 2023-05-25.

[67] C. Wohlfarth and M. Lechner, *Refractive Indices of Pure Liquids and Binary Liquid Mixtures (Supplement to III/38)* (Landolt-Börnstein: Numerical Data and Functional Relationships in Science and Technology - New Series). Springer Berlin Heidelberg, 2008, ISBN: 9783540752899. [Online]. Available: `https://books.google.com/books?id=1hsa4MDTFMkC`.

[68] C. V. Raman and K. S. Krishnan, "A new type of secondary radiation," *Nature*, vol. 121, no. 3048, pp. 501–502, 1928.

[69] A. Schulte and Y. Guo, "Laser Raman spectroscopy," *Handbook of Applied Solid State Spectroscopy*, pp. 661–688, 2006.

[70] A. Orlando *et al.*, "A comprehensive review on Raman spectroscopy applications," *Chemosensors*, vol. 9, no. 9, p. 262, 2021.

[71] R. Boyd, *Nonlinear Optics*. Elsevier Science, 2020, ISBN: 9780323850575. [Online]. Available: `https://books.google.com/books?id=sWbxDwAAQBAJ`.

[72] P. Atkins, J. De Paula, and J. Keeler, *Atkins' Physical Chemistry*. Oxford University Press, 2018, ISBN: 9780198769866. [Online]. Available: `https://books.google.com/books?id=3QpDDwAAQBAJ`.

[73] W. M. Tolles, J. W. Nibler, J. McDonald, and A. B. Harvey, "A review of the theory and application of coherent anti-stokes Raman spectroscopy (cars)," *Applied Spectroscopy*, vol. 31, no. 4, pp. 253–271, 1977.

[74] M. Chemnitz, S. Junaid, and M. A. Schmidt, "Liquid-core optical fibers—a dynamic platform for nonlinear photonics," *Laser & Photonics Reviews*, vol. 17, no. 9, p. 2 300 126, 2023.

[75] R. H. Stolen, C. Lee, and R. Jain, "Development of the stimulated Raman spectrum in single-mode silica fibers," *JOSA B*, vol. 1, no. 4, pp. 652–657, 1984.

[76] G. Agrawal, *Nonlinear Fiber Optics* (Optics and Photonics). Elsevier Science, 2012, ISBN: 9780123970237. [Online]. Available: `https://books.google.com/books?id=xNvw-GDVn84C`.

[77] R. W. Hellwarth, "Theory of stimulated Raman scattering," *Physical Review*, vol. 130, no. 5, p. 1850, 1963.

[78] C. A. Rivero, *High gain/broadband oxide glasses for next generation Raman amplifiers*. University of Central Florida, 2005.

[79] D. Long, *The Raman Effect: A Unified Treatment of the Theory of Raman Scattering by Molecules*. Wiley, 2002, ISBN: 9780471490289. [Online]. Available: `https://books.google.com/books?id=Y1TVe5BdK_UC`.

[80] A. C. Albrecht, "On the theory of Raman intensities," *The Journal of chemical physics*, vol. 34, no. 5, pp. 1476–1484, 1961.

[81] A. Albrecht and M. Hutley, "On the dependence of vibrational Raman intensity on the wavelength of incident light," *The Journal of Chemical Physics*, vol. 55, no. 9, pp. 4438–4443, 1971.

[82] D. P. Strommen, "Specific values of the depolarization ratio in Raman spectroscopy: Their origins and significance," *Journal of chemical education*, vol. 69, no. 10, p. 803, 1992.

[83] S. d. S. Porto, "Angular dependence and depolarization ratio of the Raman effect," *JOSA*, vol. 56, no. 11, pp. 1585–1589, 1966.

[84] W. L. Peticolas, "Inelastic light scattering and the Raman effect," *Annual Review of Physical Chemistry*, vol. 23, no. 1, pp. 93–116, 1972.

[85] W. R. Fenner, H. A. Hyatt, J. M. Kellam, and S. Porto, "Raman cross section of some simple gases," *JOSA*, vol. 63, no. 1, pp. 73–77, 1973.

[86] J.-G. Skinner and W. Nilsen, "Absolute Raman scattering cross-section measurement of the 992 cm- 1 line of benzene," *JOSA*, vol. 58, no. 1, pp. 113–119, 1968.

[87] J. Grun, A. McQuillan, and B. Stoicheff, "Intensity and gain measurements on the stimulated Raman emission in liquid o 2 and n 2," *Physical Review*, vol. 180, no. 1, p. 61, 1969.

[88] Y. Kato and H. Takuma, "Experimental study on the wavelength dependence of the Raman scattering cross sections," *The Journal of Chemical Physics*, vol. 54, no. 12, pp. 5398–5402, 1971.

[89] G. Placzek, "The rayleigh and Raman scattering translated from: Handbuch der radiologie, ed. erich marx, akademische verlagsgesellschaft vi, 2, 209-374, leipzig," 1934.

[90] M. Colles and J. Griffiths, "Relative and absolute Raman scattering cross sections in liquids," *The Journal of Chemical Physics*, vol. 56, no. 7, pp. 3384–3391, 1972.

[91] Y. Udagawa, N. Mikami, K. Kaya, and M. Ito, "Absolute intensity ratios of Raman lines of benzene and ethylene derivatives with 5145 Å and 3371 Å excitation," *Journal of Raman Spectroscopy*, vol. 1, no. 4, pp. 341–346, 1973.

[92] H. Schrötter and H. Klöckner, "Raman scattering cross sections in gases and liquids," *Raman spectroscopy of gases and liquids*, pp. 123–166, 1979.

[93] C. D. Allemand, "Depolarization ratio measurements in Raman spectrometry," *Applied Spectroscopy*, vol. 24, no. 3, pp. 348–353, 1970.

[94] M. Maier, W. Kaiser, and J. Giordmaine, "Backward stimulated Raman scattering," *Physical Review*, vol. 177, no. 2, p. 580, 1969.

[95] H. Görner, M. Maier, and W. Kaiser, "Raman gain in liquid-core fibers," *Journal of Raman Spectroscopy*, vol. 2, no. 4, pp. 363–371, 1974.

[96] R. L. Carman, F. Shimizu, C. Wang, and N. Bloembergen, "Theory of stokes pulse shapes in transient stimulated Raman scattering," *Physical Review A*, vol. 2, no. 1, p. 60, 1970.

[97] D. Von Der Linde, "Picosecond interactions in liquids and solids," *Ultrashort Light Pulses: Picosecond Techniques and Applications*, pp. 203–273, 1977.

[98] L. Schneebeli *et al.*, "Measurement of the Raman gain coefficient via inverse Raman scattering," *JOSA B*, vol. 30, no. 11, pp. 2930–2939, 2013.

[99] M. O. Trulson and R. A. Mathies, "Raman cross section measurements in the visible and ultraviolet using an integrating cavity: Application to benzene, cyclohexane, and cacodylate," *The Journal of chemical physics*, vol. 84, no. 4, pp. 2068–2074, 1986.

[100] N. Abe, M. Wakayama, and M. Ito, "Absolute Raman intensities of liquids," *Journal of Raman Spectroscopy*, vol. 6, no. 1, pp. 38–41, 1977.

[101] G. Eckhardt and W. G. Wagner, "On the calculation of absolute Raman scattering cross sections from Raman scattering coefficients," *Journal of Molecular Spectroscopy*, vol. 19, no. 1-4, pp. 407–411, 1966.

[102] G. Bisson, G. Bret, M. Denariez, F. Gires, G. Mayer, and M. Paillette, "L'émission Raman stimulée sans cavité résonnante extérieure," *Journal de Chimie Physique*, vol. 64, pp. 197–208, 1967.

[103] T. Damen, R. Leite, and S. Porto, "Angular dependence of the Raman scattering from benzene excited by the he-ne cw laser," *Physical Review Letters*, vol. 14, no. 1, p. 9, 1965.

[104] K. Schomacker, J. Delaney, and P. Champion, "Measurements of the absolute Raman cross sections of benzene," *The Journal of chemical physics*, vol. 85, no. 8, pp. 4240–4247, 1986.

[105] J. Van Vleck, "On the vibrational selection principles in the Raman effect," *Proceedings of the National Academy of Sciences*, vol. 15, no. 9, pp. 754–764, 1929.

[106] H. Szymanski, *Raman Spectroscopy: Theory and Practice*. Springer US, 2012, ISBN: 9781468430264. [Online]. Available: `https://books.google.com/books?id=1EPyngEACAAJ`.

[107] *Standard Spectra*, `https://www.chem.ualberta.ca/~mccreery/ramanmaterials.html`, Accessed: 2023-10-29.

[108] W. Clements and B. Stoicheff, "Raman linewidths for stimulated threshold and gain calculations," *Applied Physics Letters*, vol. 12, no. 8, pp. 246–248, 1968.

[109] *Combination of Profiles*, `https://phys.libretexts.org/Bookshelves/Astronomy_Cosmology/Stellar_Atmospheres_(Tatum)/10%3A_Line_Profiles/10.04%3A_Combination_of_Profiles`, Accessed: 2023-10-29.

[110] K. Tanabe, "Raman linewidth study of rotational motion of benzene in aqueous solution," *Spectrochimica Acta Part A: Molecular Spectroscopy*, vol. 38, no. 1, pp. 119–121, 1982.

[111] F. McClung and D. Weiner, "Measurement of Raman scattering cross sections for use in calculating stimulated Raman scattering effects," *JOSA*, vol. 54, no. 5, pp. 641–643, 1964.

[112] K. Tanabe, "Raman line width study of rotational motion of cyclohexane in aqueous solution," *The Journal of Physical Chemistry*, vol. 86, no. 3, pp. 319–321, 1982.

[113] A. Dogariu and D. J. Hagan, "Low frequency Raman gain measurements using chirped pulses," *Optics Express*, vol. 1, no. 3, pp. 73–76, 1997.

[114] L. Shan, G. Pauliat, G. Vienne, L. Tong, and S. Lebrun, "Design of nanofibres for efficient stimulated Raman scattering in the evanescent field," *Journal of the European Optical Society-Rapid publications*, vol. 8, 2013.

[115] R. L. Sutherland, *Handbook of nonlinear optics*. CRC press, 2003.

[116] D. Von der Linde, M. Maier, and W. Kaiser, "Quantitative investigations of the stimulated Raman effect using subnanosecond light pulses," *Physical review*, vol. 178, no. 1, p. 11, 1969.

[117] M. Bass *et al.*, *Handbook of Optics, Third Edition Volume IV: Optical Properties of Materials, Nonlinear Optics, Quantum Optics (set)* (Handbook of Optics). McGraw Hill LLC, 2009, ISBN: 9780071629294. [Online]. Available: `https://books.google.com/books?id=1CES2tOBwikC`.

[118] J. C. R. Reis, I. M. Lampreia, Â. F. Santos, M. L. C. Moita, and G. Douhéret, "Refractive index of liquid mixtures: Theory and experiment," *ChemPhysChem*, vol. 11, no. 17, pp. 3722–3733, 2010.